

## Spatial and temporal evolution of injected CO<sub>2</sub> at the Sleipner Field, North Sea

F. C. Boait,<sup>1</sup> N. J. White,<sup>1</sup> M. J. Bickle,<sup>1</sup> R. A. Chadwick,<sup>2</sup> J. A. Neufeld,<sup>3,4</sup> and H. E. Huppert<sup>3</sup>

Received 28 June 2011; revised 13 January 2012; accepted 23 January 2012; published 13 March 2012.

[1] Time-lapse, three-dimensional (3D) seismic surveys have imaged an accumulation of injected CO<sub>2</sub> adjacent to the Sleipner field in the North Sea basin. The changing pattern of reflectivity suggests that CO<sub>2</sub> accumulates within a series of interbedded sandstones and mudstones beneath a thick caprock of mudstone. Nine reflective horizons within the reservoir have been mapped on six surveys acquired between 1999 and 2008. These horizons have roughly elliptical planforms with eccentricities ranging between two and four. In the top half of the reservoir, horizon areas grow linearly with time. In the bottom half, horizon areas initially grow linearly for about eight years and then progressively shrink. The central portions of deeper reflective horizons dim with time. Amplitude analysis of horizons above, within, and below the reservoir show that this dimming is not solely caused by acoustic attenuation. Instead, it is partly attributable to CO<sub>2</sub> migration and/or CO<sub>2</sub> dissemination, which reduce the impedance contrast between sandstone and mudstone layers. Growth characteristics and permeability constraints suggest that each horizon grows by lateral spreading of a gravity current. This model is corroborated by the temporal pattern of horizon velocity pushdown beneath the reservoir. Horizon shrinkage may occur if the distal edge of a CO<sub>2</sub>-filled layer penetrates the overlying mudstone, if the buoyant plume draws CO<sub>2</sub> upward, or if the effective permeability of deeper mudstone layers increases once interstitial brine has been expelled. Topographic control is evident at later times and produces elliptical planforms, especially toward the top of the reservoir. Our results show that quantitative mapping and analysis of time-lapse seismic surveys yield fluid dynamical insights which are testable, shedding light on the general problem of CO<sub>2</sub> sequestration.

**Citation:** Boait, F. C., N. J. White, M. J. Bickle, R. A. Chadwick, J. A. Neufeld, and H. E. Huppert (2012), Spatial and temporal evolution of injected CO<sub>2</sub> at the Sleipner Field, North Sea, *J. Geophys. Res.*, *117*, B03309, doi:10.1029/2011JB008603.

### 1. Introduction

[2] The Sleipner field in the North Sea is a site of a long-running carbon capture and storage project [Arts *et al.*, 2008; Chadwick and Noy, 2010]. At the Sleipner platform, CO<sub>2</sub> is removed from natural gas, which is produced from a nearby field [Baklid *et al.*, 1996]. Unwanted CO<sub>2</sub> is injected into the Utsira Sand, a porous saline reservoir which extends over a large region (400 × 100 km<sup>2</sup> [Gregerson, 1998]). Close to the injection point, the top of this reservoir is at a depth of 800 m [Zweigel *et al.*, 2004]. CO<sub>2</sub> injection commenced in 1996 [Baklid *et al.*, 1996]. The reservoir has been imaged by one pre-injection and six post-injection marine seismic surveys, which have yielded excellent 3D acoustic images

[Chadwick *et al.*, 2005]. A total of seven time-lapse seismic surveys demonstrate that CO<sub>2</sub> has spread into nine horizons up to the top of the Utsira Sand. These images reveal how the reflectivity of each horizon has changed as a function of space and time.

[3] Previously, Bickle *et al.* [2007] analyzed seismic images from the 1999, 2001 and 2002 surveys. They showed that the area of each CO<sub>2</sub>-filled horizon increased linearly as a function of time. This observation is consistent with axisymmetric spreading of a porous gravity current with constant input flux along a horizontal surface [Lyle *et al.*, 2005]. In contrast, Singh *et al.* [2010] suggest that horizon growth is controlled by reservoir topography. Our study has three main aims. First, we extend previous analyses by detailed mapping of an updated time-lapse inventory. Secondly, we investigate the causes of amplitude dimming and horizon pushdown within, and beneath, the reservoir. Thirdly, we use analytical and numerical models to assess the relative importance of gravity spreading and topographic control within the reservoir. We are especially interested in the following questions. How does CO<sub>2</sub> migrate vertically and horizontally through the reservoir? What is the amount and distribution of CO<sub>2</sub>

<sup>1</sup>Bullard Laboratories, Cambridge, UK.

<sup>2</sup>British Geological Survey, Keyworth, UK.

<sup>3</sup>Institute of Theoretical Geophysics, Department of Applied Mathematics and Theoretical Physics, Cambridge, UK.

<sup>4</sup>BP Institute, Bullard Laboratories, Cambridge, UK.

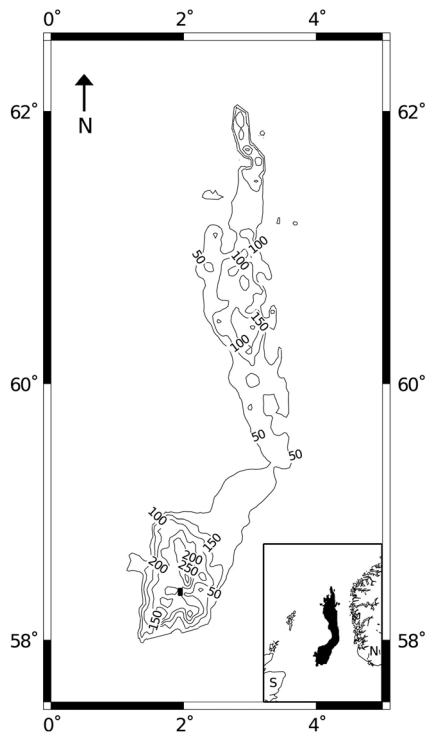


**Figure 1.** Mercator projection which shows distribution of Utsira Sand in eastern North Sea. Numbered contours show thickness in meters; small black rectangle shows dimensions of time-lapse seismic survey. Inset: location of main figure; black shading shows extent of Utsira Sand. S, Scotland, N, Norway.

within and between horizons? Is dimming and shrinkage of the lowest horizons real and, if so, what are the causes?

## 2. Background

[4] The Utsira Sand was deposited during Pliocene times in the eastern part of the North Sea basin [Gregerson *et al.*, 1997; Head *et al.*, 2004]. Adjacent to the Sleipner field, this sandstone formation is 200–300 m thick [Chadwick *et al.*, 2004] (Figure 1). It is now buried at a depth of 800–1000 m and consists of unconsolidated sand with 35–40% porosity [Zweigel *et al.*, 2001]. Nearby wireline logs show that the sandstone has a uniform composition with a permeability of  $1\text{--}3 \times 10^{-12} \text{ m}^2$  [Chadwick *et al.*, 2004]. There is no direct evidence for anisotropic permeability. Within the Utsira Sand, thin (1–2 m thick) mudstone layers act as semi-permeable barriers to fluid flow. The ultimate seal is the thick overlying Nordland Shale [Isaksen and Tonstad, 1989; Zweigel *et al.*, 2000].

[5] Injection started in 1996 and ramped up to a rate of approximately one million tonnes of CO<sub>2</sub> per year [Korbøl and Kaddour, 1996] (Figure 2b). The injection rate has fluctuated, with a small dip during 2004. CO<sub>2</sub> is injected at a depth of 1012 m below sea level (bsl) through a 2 km long deviated well which penetrates the lower half of the reservoir [Baklid *et al.*, 1996] (Figure 2a). CO<sub>2</sub> migrates up through the reservoir to the base of the Nordland Shale at 800 m depth [Arts *et al.*, 2004]. By 2008, more than 10 million tonnes has

been sequestered [Chadwick *et al.*, 2010]. For a density of  $700 \text{ kg m}^{-3}$ , the average input flux,  $Q$ , is  $0.04 \text{ m}^3 \text{ s}^{-1}$ .

[6] Temperature and pressure conditions determine the sub-surface properties of the injected CO<sub>2</sub>. There is no active temperature monitoring of the reservoir. Prior to injection, a single downhole measurement of 37°C was obtained at a depth of 1056 m. Subsequently, thermal modeling based on well-constrained temperature measurements from the deeper Sleipner gas reservoir suggests that the temperature at the injection depth (i.e. 1090 m bsl) could be as high as 41°C [Chadwick and Noy, 2010]. In late 2007, large-scale water production from the Utsira Sand commenced at the Volve field, a few kilometers to the north of the Sleipner field. Here, a near-equilibrium temperature of 27.7°C was recorded at a depth of 768 m bsl. A temperature of 32.2°C was recorded in water produced from a reservoir interval at 822–1009 m depth bsl. These additional values support the original downhole measurement at the Sleipner field.

[7] Pressure at the wellhead was  $\sim 6.2 \text{ MPa}$  between 1997 to 2001 and has been  $\sim 6.4 \text{ MPa}$  after 2005 [Chadwick *et al.*, 2009b]. In the reservoir, the density of CO<sub>2</sub> cannot be reliably obtained and indirect estimates are used [Lindeberg *et al.*, 2009]. Gravity measurements suggest that the density is between  $550 \text{ and } 750 \text{ kg m}^{-3}$ , which is much less than that of brine [Nooner *et al.*, 2007]. Density could be slightly lower since 1–2 % of the injected material consists of lighter impurities, notably methane [Chadwick *et al.*, 2009b]. In the absence of down-hole gauges within the injection well, the temperature of CO<sub>2</sub> at the base of the well is estimated as 48°C and pressure is assumed to be hydrostatic ( $\sim 10.5 \text{ MPa}$  [Alnes *et al.*, 2011]). Under these conditions, the density is  $485 \pm 10 \text{ kg m}^{-3}$  at the perforation. Its value should increase with distance away from the well since CO<sub>2</sub> will cool on contact with the Utsira Sand and a density maximum of  $\sim 710 \text{ kg m}^{-3}$  is expected [Alnes *et al.*, 2011]. In summary, CO<sub>2</sub> within the Utsira Sand is at supercritical conditions. Since temperature drops by  $\sim 6^\circ\text{C}$  through the reservoir section, we are confident that CO<sub>2</sub> directly beneath the Nordland Shale remains in the liquid phase [Han *et al.*, 2010].

[8] The reliability of our study is predicated upon a consistent standard of seismic acquisition and processing over seven seismic surveys (Table 1). Acquisition parameters are generally similar across all surveys (i.e. source array, source volume, streamer length, fold of cover). There are two notable differences. The 2004 survey was acquired at 90° to other surveys, and the 2002 survey does not quite cover the eastern edge of the plume. Seismic processing was carried out by various seismic contractors, often using different algorithms and implementations. Since only particular surveys have been processed in an identical way, we have used information from the relevant processing reports to guide our interpretation strategy. For example, detailed comparisons can be made between the 1994, 2001, 2006 and 2008 surveys but we have not exploited amplitude maps from the anomalously oriented 2004 survey. We have also avoided using the 1999 and 2002 surveys for detailed comparisons because their pre- and post-stack processing sequences differ in significant ways (O. Eiken, written communication, 2008). In the absence of reliable far-field measurements, the frequency bandwidth of the source can be estimated in two ways. First, general frequency content can be measured directly from

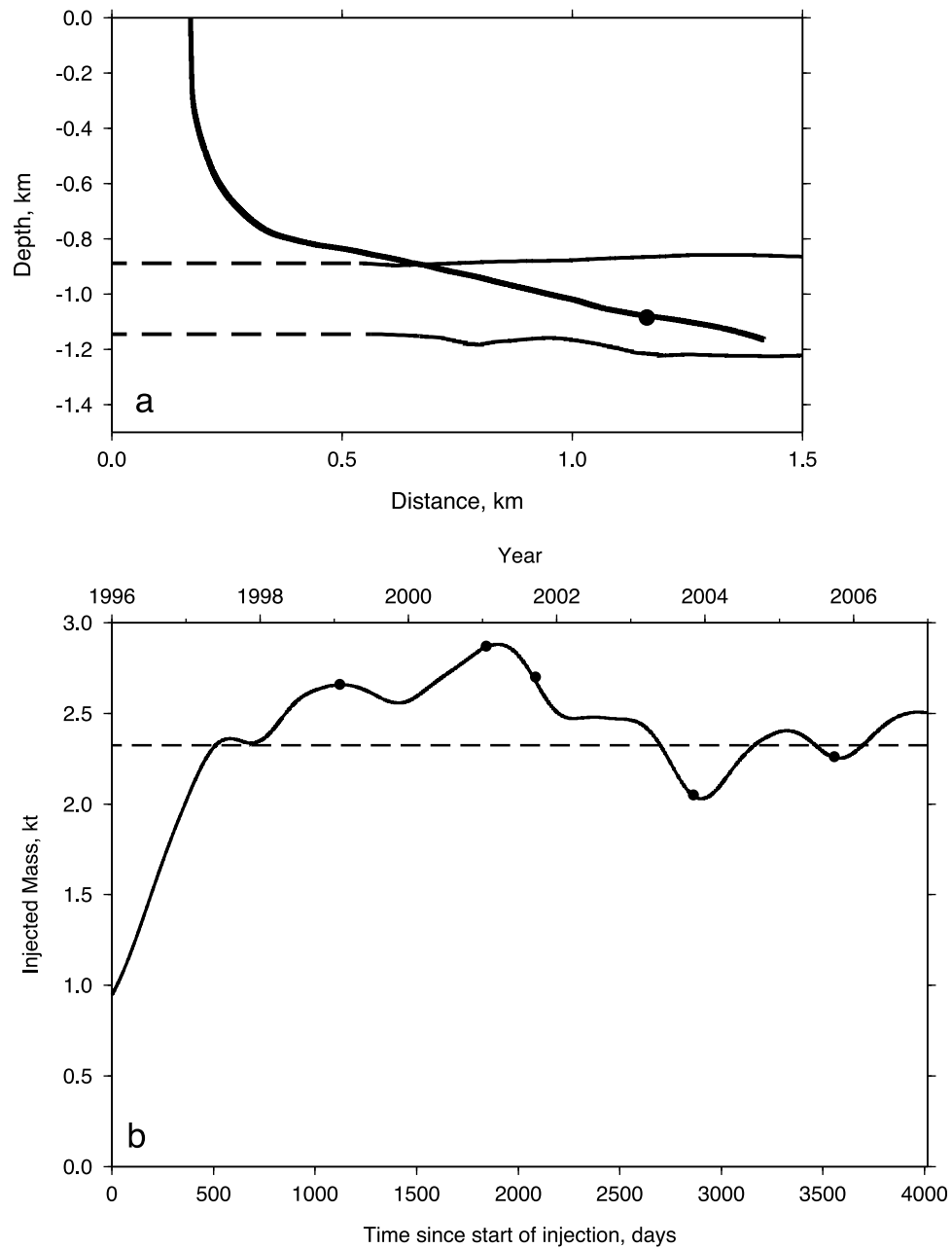


**Figure 2.** (a) Trajectory of injection well which pumps CO<sub>2</sub> into Utsira Sand at depth of 1012 m; solid line shows projected trace of well; solid circle shows injection point; solid and dashed horizons show top and bottom of Utsira Sand. (b) Solid curve shows injected mass of CO<sub>2</sub> as a function of time (daily record smoothed using Gaussian function with 2 year width); dashed curve shows average injected mass; solid circles show timing of 1999, 2001, 2002, 2004, and 2006 seismic surveys. Note increase between 1996 and 1998 and decrease during 2004.

**Table 1.** Acquisition Parameters for Sleipner

Parameter	Year						
	1994	1999	2001	2002	2004	2006	2008
Shotpoint interval, m	18.75 ff <sup>a</sup>	12.5	12.5 ff <sup>a</sup>	18.75	18.75	18.75 ff <sup>a</sup>	18.75
Shooting direction	N-S	N-S	N-S	N-S	E-W	N-S	N-S
Array type	dual	dual	dual	dual	single	dual	dual
Array Separation, m	50	50	50	50	n.a.	50	50
Volume, inches <sup>3</sup>	3400	3542	3397	3147	4280	3660	3660
Depth, m	6	6	6	6	6	6	6
Air pressure, pounds/inch <sup>2</sup>	2000		2000		2000	2000	
Streamer length, m	3000	3600	1500	3600	4500	3600	3000
Number of Streamers	5	4	4	6	10	8	9
Streamer separation, m	100	100	100	100	37.5	100	50
Group interval, m	12.5	12.5	12.5	12.5	12.5	12.5	12.5
Streamer depth, m	8	8	8	8	8	8	8
Low-cut filter, Hz@dB/oct	3.4 @18	3 @18	3 @18	3 @ 18	3.4 @t 18	3 @ 12	3 @ 12
High-cut filter, Hz@dB/oct	180 @ 70	180 @ 70	200 @ 406	180 @ 72	206 @276	206 @ 276	206 @ 276
Sample interval, ms	2	2	2	2	2	2	2
Record length, ms	5500	4500	4500	6000	6000	6000	6000

<sup>a</sup>In this table ff = flipflop source.

stacked cubes. For example, frequency analysis of the 2006 survey shows that it has a dominant bandwidth of about 20–50 Hz. Secondly, an approximate source wavelet has been extracted from the same survey, which suggests that the peak frequency is 30 Hz [Chadwick *et al.*, 2005].

### 3. Seismic Imaging

#### 3.1. Horizon Mapping

[9] The baseline (i.e. 1994) survey delineates the pre-injection reservoir geometry (Figure 3). Overall structure of the reservoir is determined by the shape of a reflective boundary between the Utsira Sand and the overlying Nordland Shale (TU). This boundary forms a low-amplitude dome with a diameter of  $\sim 1.2$  km, a height above spill-point of 12 m, and a maximum slope of  $\sim 1.2^\circ$  [Zweigel *et al.*, 2004]. The base of the reservoir is defined by a reflective boundary between the Utsira Sand and the underlying Hordland Shale (BU). This boundary is locally difficult to map because it has significant relief, which was probably generated by post-depositional, soft-sediment deformation [Galloway, 2002]. Within the Hordland Shale, a bright, flat reflection is visible, which we have called the IntraHordland horizon (IH). The reservoir itself consists of an interbedded stack of sandstone and mudstone layers, which have thicknesses of between 10 and 40 m and 1–2 m, respectively [Chadwick *et al.*, 2004; Zweigel *et al.*, 2000]. The highest intrareservoir mudstone is 5 m thick, although the ultimate seal is the Nordland Shale, which is  $\sim 200$  m thick [Zweigel *et al.*, 2000]. Coherency analysis of the baseline survey indicates that no significant faulting displaces middle and upper units of the reservoir, in agreement with previous studies [Zweigel *et al.*, 2004].

[10] On the six post-injection surveys, a growing CO<sub>2</sub> plume is manifest as a series of bright reflections, each of which is generated by changes in acoustic impedance at boundaries between the thicker sandstones and the thinner mudstones [Arts *et al.*, 2004] (Figure 3). CO<sub>2</sub> is expected to accumulate with significant saturations toward the top of each sandstone layer, which causes the acoustic impedance contrast with the overlying mudstone cap to increase. Each reflection has been carefully picked and nine discrete

horizons, numbered 1–9 from bottom to top of plume, have been identified and mapped [Chadwick *et al.*, 2004]. We have remapped all nine horizons to generate a series of self-consistent amplitude maps (Figure 4). The edge of each horizon was chosen by identifying loci where amplitude reduces to its reservoir background value on the baseline survey. We have also mapped prominent reflective boundaries above and below the reservoir. Boundaries above the reservoir should be unchanged across all surveys, subject to changes in acquisitional geometry and processing parameters. Boundaries beneath the reservoir exhibit velocity pushdown (i.e. additional time delay) since CO<sub>2</sub> has a lower acoustic velocity than brine [Chadwick *et al.*, 2005; Zweigel *et al.*, 2000] (Figure 3). Thus, the BU and IH horizons can be used to measure the growth of pushdown produced by the progressive accumulation of CO<sub>2</sub>. Combined changes in seismic amplitude and extent of each horizon within the reservoir, as well as pushdown of sub-reservoir horizons, constrain the amount and distribution of CO<sub>2</sub> within the reservoir.

[11] We have not attempted to carry out pre- or post-stack acoustic impedance inversions for three reasons. First, the survey area is not locally calibrated by any borehole. Secondly, it is generally accepted that seismic amplitudes within the CO<sub>2</sub> plume are affected by frequency tuning. Thirdly, we believe that careful mapping of post-stack data reveals important observations which would be obscured by sets of uncalibrated inverse models. The interested reader is referred to Chadwick *et al.* [2010], who have carried out preliminary pre- and post-stack inversions, which do not alter our principal conclusions.

#### 3.2. Horizon Reflectivity and Planform

[12] A set of 54 amplitude maps documents horizon growth (Figure 4). In many cases, a three-stage evolution occurs. In the first stage, when a horizon starts to grow, it spreads laterally and its amplitude brightens. During the second stage, its central amplitude may dim, even though the amplitude toward the edges may continue to brighten. In the final stage, a horizon may stop growing and even shrink, accompanied by an overall decrease of amplitude. Each stage is reached by different horizons at different times.

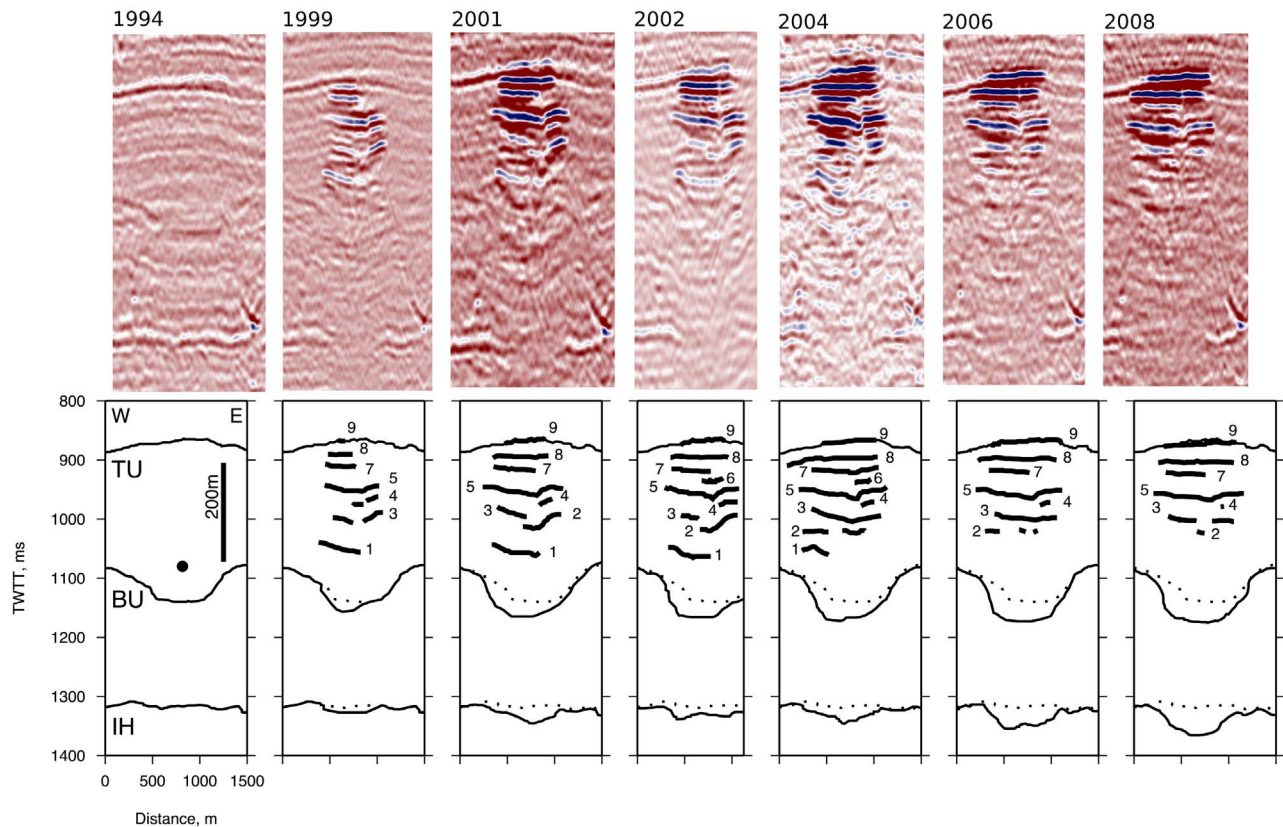


**Figure 3.** Set of vertical slices through 7 time-lapse seismic volumes. (top) Uninterpreted slices showing growth of CO<sub>2</sub>-filled horizons. Note change in reflectivity and pushdown of layers beneath plume. (bottom) Line drawing interpretations. Numbered solid curves 1–9 mapped horizons; solid circle on 1994 slice shows the injection point; thinner lines labeled TU, BU and IH are top Utsira Sand, base Utsira Sand, and intraHordlandformation, respectively; dotted lines are BU and IH horizons from 1994 survey. Note growth of pushdown through time.  $\sim 3$  times vertical exaggeration.

The deepest horizons (1–4) and horizon 7 reach the third stage by 2004, while the middle horizons (5 and 6) reach the second stage by 2004. The shallowest horizons (8 and 9) develop second stage features after 2006.

[13] Planforms of the horizons differ. For example, horizons 5, 7, 8 and 9 are highly coherent and show no evidence of patchiness. Other horizons are initially coherent but later break up into a series of discrete patches (e.g. horizons 4 and 6). Most horizons, including the fragmented ones, have elliptical planforms with remarkably consistent values of the ellipticity,  $e$  (Figure 5). Long axes of these ellipses generally trend NNE-SSW. Horizons 1 and 2 have an almost constant value of  $e \sim 2$  (Figure 6). The ellipticity of horizon 3 grows from 1 to 3 over 12 years. In the middle of the plume, horizons 4, 5 and 6 have  $e \sim 4$  although the ellipticity of horizon 6 grows rapidly between 2001 and 2002. Toward the top of the reservoir, horizons 7 and 8 have  $e \sim 2$  with some evidence of a decrease with time. The ellipticity of horizon 9 grows from  $\sim 2$  to  $\sim 4$  between 2002 and 2006. These uniform ellipticities might be controlled by a combination of the structural configuration of the reservoir and the inferred existence of NNE-SSW trending anisotropic permeability [Chadwick and Noy, 2010].

[14] Horizon reflectivity is the principal means of monitoring CO<sub>2</sub> accumulation and flow within the reservoir. It is

generally agreed that layers of CO<sub>2</sub> are trapped under 1–2 m thick mudstones which are inferred from wireline logs of adjacent boreholes, which penetrate the Utsira Sand [Zweigel *et al.*, 2000]. These mudstones are too thin to be seismically imaged, given a dominant frequency bandwidth of 20–50 Hz. They are also too discontinuous to be mapped using adjacent, widely spaced boreholes. The mudstone layer, which caps horizon 8, is 5 m thick where it is intersected by the injection well and by borehole 15/9–13 [Zweigel *et al.*, 2000]. The usefulness of seismic imaging within a reservoir is limited in two important ways. First, if the acoustic velocity of brine-saturated reservoir rocks is  $\sim 2050$  m/s, the vertical resolution is  $\sim 17$  m, which suggests that the internal structure of this reservoir is just below the limits of resolution [Arts *et al.*, 2004]. Note that vertical resolution is  $\sim 12$  m for CO<sub>2</sub>-saturated rocks. Secondly, the ability to transmit acoustic energy into the lower part of the reservoir diminishes as overlying reflective horizons brighten.

### 3.3. Velocity Pushdown Calculations

[15] Velocity pushdown beneath the reservoir provides a useful estimate of the cumulative mass and distribution of CO<sub>2</sub> within a reservoir [Chadwick *et al.*, 2005]. Pushdown arises because CO<sub>2</sub>-bearing sandstone has a significantly slower acoustic velocity than brine-bearing sandstone. The

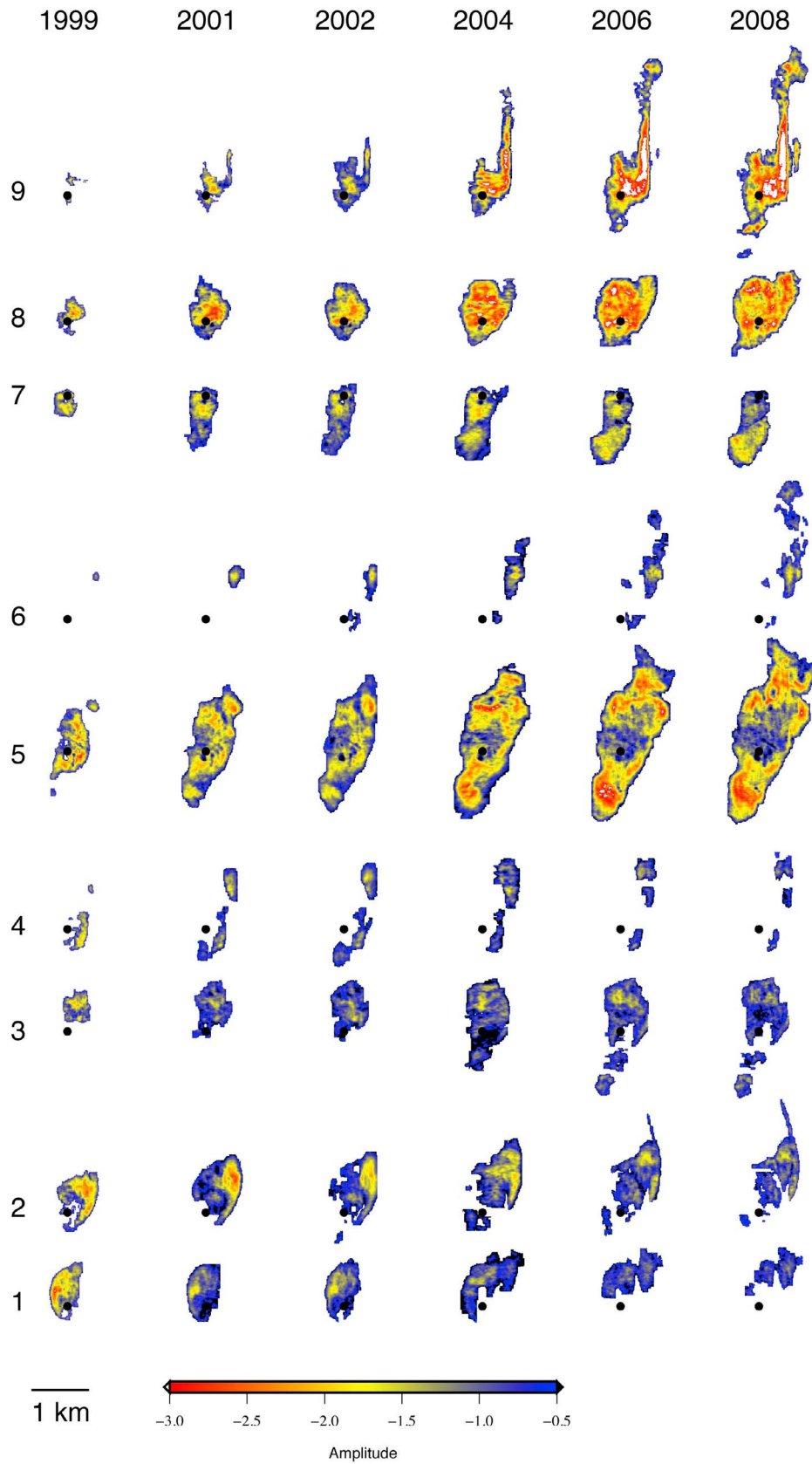


**Figure 4.** Horizontal slices through time-lapse seismic data showing amplitude variation for 1–9 horizons as function of time (see Figure 3 for vertical position of each horizon). Warmer and colder colors show stronger and weaker amplitudes; solid circle shows the injection point.

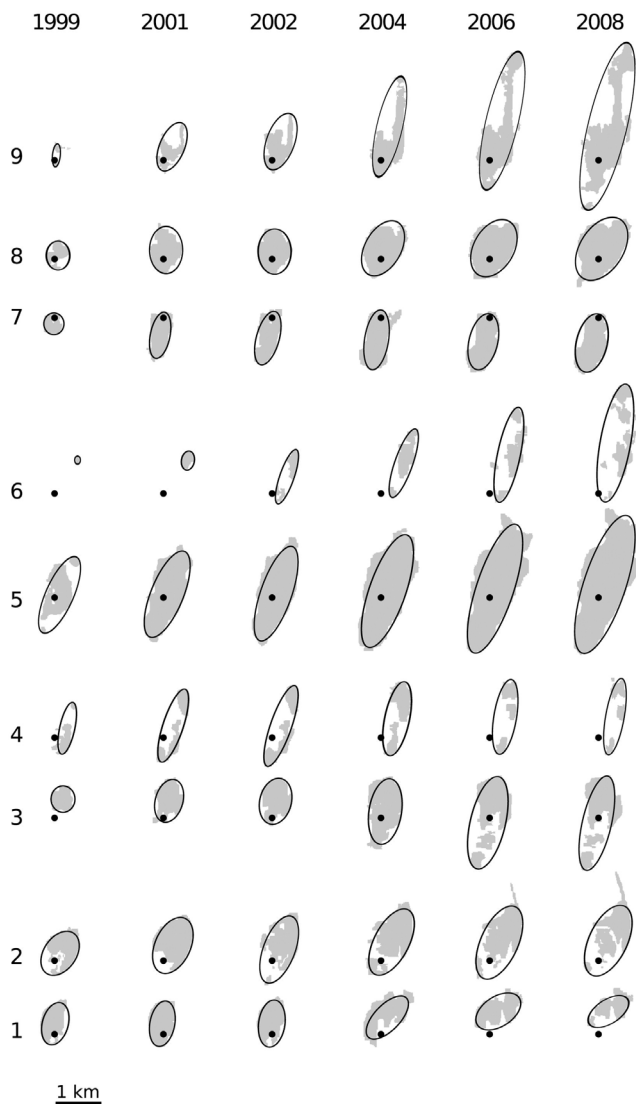


**Figure 5.** Ellipses fitted to horizon planforms. Gray shading shows mapped planforms; solid circles show injection points; solid lines show inscribed ellipses fitted by eye.

amount of pushdown is determined by the cumulative thickness and distribution of CO<sub>2</sub>-bearing layers, by CO<sub>2</sub> saturation, and by temperature- and pressure-dependent CO<sub>2</sub> properties. For a given survey, horizon pushdown is measured with respect to that horizon's shape on the baseline survey. Here, we measured pushdown of the BU and IH horizons beneath the reservoir. Horizon pushdown also occurs within the reservoir. However, it only becomes visible on the post-injection surveys and so the baseline survey cannot be used as a reference.

[16] The BU and IH horizons have been mapped on all seven surveys and in each case pushdown increases steadily with time (Figure 3). Areal changes of pushdown as a function of time are shown in Figure 6. Pushdown (i.e. the cumulative mass of CO<sub>2</sub>) is greater beneath the center of the plume. There are two plausible mechanisms for this observation. First, the thickness of one or more CO<sub>2</sub>-saturated layers decreases from the center to the edge of the plume. Secondly, some proportion of CO<sub>2</sub> may be disseminated

between the reflective horizons at the center of the plume. It is possible that a combination of both mechanisms play a role.

[17] Since pushdown is a proxy for the cumulative mass of CO<sub>2</sub> within the reservoir, it is helpful to compare it with the cumulative amplitude of reflective horizons, which has a less straightforward relationship with the mass and distribution of CO<sub>2</sub>. Figure 7 shows the spatial and temporal distribution of cumulative amplitude of all 9 horizons for surveys 2001, 2004, 2006 and 2008. Between 2001 and 2006, the cumulative amplitude increased but by 2008 the amplitude at the center has decreased. Since pushdown for BU and IH increases between 2006 and 2008, the decrease in cumulative amplitude at the center cannot be caused by mass reduction.

[18] The thickness of CO<sub>2</sub> required to generate the observed pushdown can be estimated provided that the velocity and saturation of CO<sub>2</sub> in the reservoir is known. If the distribution of CO<sub>2</sub> is homogeneous, then acoustic velocity is insensitive to saturations greater than 30% and the saturation of CO<sub>2</sub> within a layer cannot be seismically determined [Gassmann, 1951; Carcione et al., 2006]. Saturation within the CO<sub>2</sub>-rich horizons is probably greater than 30%, except within a few centimeters of a horizon's base [Chadwick et al., 2005]. Golding et al. [2011] show that the saturation profiles strongly depend upon the pore size distribution within the reservoir rock. If each layer has an average saturation of 80% and if the total injected mass of CO<sub>2</sub> is confined to the zone where reflective horizons occur, each layer is 5–8 m thick, given a porosity of 37% and the density of CO<sub>2</sub> (i.e. 500–700 kg m<sup>-3</sup>). For a saturation of 40%, which is required to lower effective permeability by a factor of 0.1, layers thicken to 10–14 m [Bickle et al., 2007; M. J. Golding et al., Capillary effects on the spreading of axisymmetric, two-phase gravity currents in porous media, submitted to *Journal of Fluid Mechanics*, 2012].

[19] The effective thickness of each CO<sub>2</sub> layer can be estimated by matching the number of reflective horizons at a given location to pushdown of BU and IH underneath the CO<sub>2</sub> plume (Figure 8). The observed pushdown of BU and IH is divided by the number of overlying reflective horizons at each point, which yields an average pushdown per layer. If the distribution of CO<sub>2</sub> is homogeneous and if acoustic velocity is insensitive to saturations greater than 30% [Gassmann, 1951; Carcione et al., 2006], we can convert average pushdown per layer into average thickness per layer. Calculated thicknesses are sometimes as great as 20 m (Figure 8). One-dimensional reflectivity modeling shows that a tuned wavelet splits into two separate reflections when the layer thickness is greater than ~18 m. We conclude that the observed pushdown cannot be entirely accounted for by mappable horizons and that a small additional source of pushdown exists. This source could be low saturation CO<sub>2</sub>, which is distributed between the higher saturation horizons.

[20] There is also a discrepancy between the position of the maximum observed pushdown and the locus of the cumulative number of overlying reflective layers (Figure 8). This spatial discrepancy suggests that some disseminated CO<sub>2</sub> occurs away from mappable horizons. Maximum pushdown for the BU horizon grows from 42 to 48 ms between 2001 and 2008. This value corresponds to a CO<sub>2</sub> thickness increase of 15 m for a homogeneous saturation. A smaller value of 7 m is obtained from pushdown of the IH horizon.

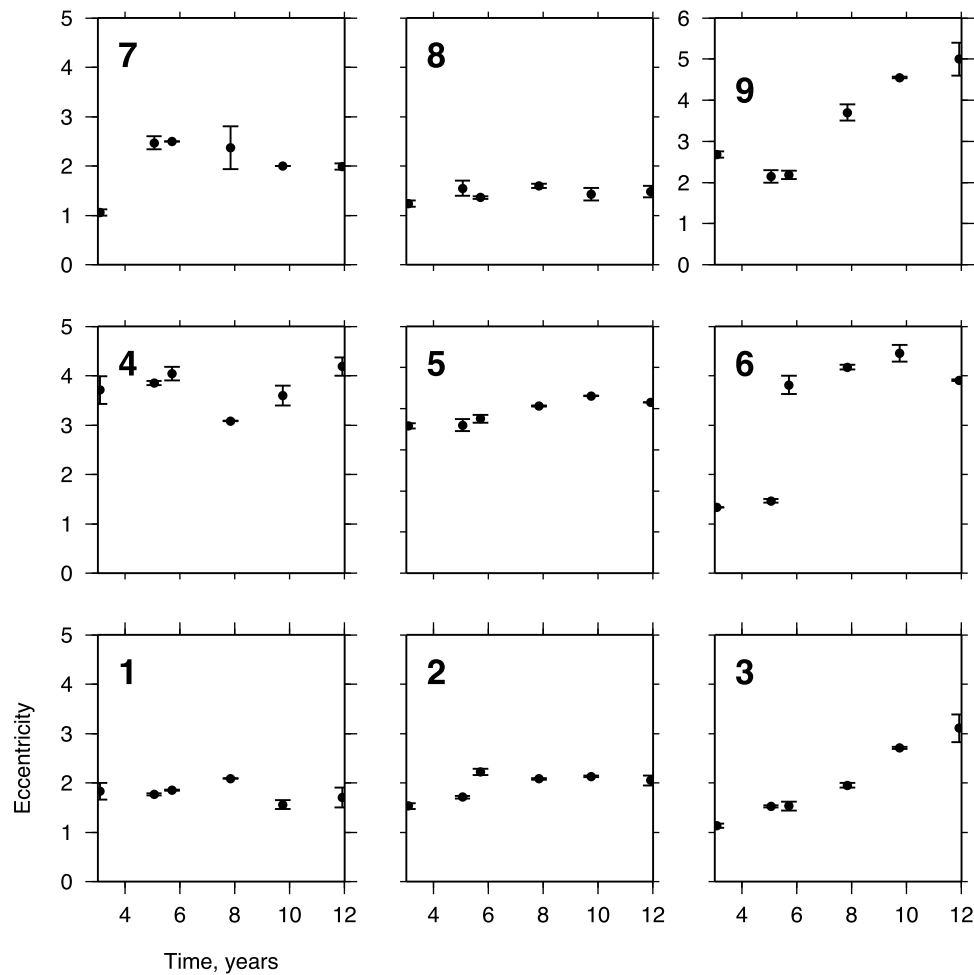


**Figure 6.** Eccentricity plotted as a function of time for all nine horizons. Eccentricity was estimated by inscribing ellipses around 54 amplitude maps (Figure 5). Year 3 is 1999, year 12 is 2008.

### 3.4. Reflectivity Dimming

[21] Figure 4 shows that dimming of reflectivity is common, especially in the bottom half of the reservoir. For example, horizons 1–4 are initially bright but progressively dim with time, albeit at different rates. Almost from its inception, horizon 5 begins to dim along its western margin, which is directly above the injection point. This dimming gradually migrates toward the horizon’s center. The top 4 horizons exhibit less dimming, although the amplitude at the center of horizon 8 decreases. Importantly, horizon 9 dims even though temporal changes in acoustic transmission are not expected at the top of the reservoir.

[22] Dimming is usually caused by changes in either reflection coefficient or signal strength. An obvious cause of signal strength reduction is the progressive decrease in acoustic transmission beneath a brightening horizon. This reduction is caused by a drop in acoustic transmission at overlying interfaces and by frequency-dependent (i.e. intrinsic) attenuation, which is a true energy loss mechanism caused by, for example, induced fluid movement within the pore space as an acoustic wave passes through a formation. Such forms of dimming might account for the decrease in reflectivity of horizons 1–4 [Chadwick *et al.*, 2004].

Similarly, a decrease in reflectivity at the center of horizon 5 might be caused by the increased reflectivity of horizon 8. Any reduction in signal strength can also be affected by mode conversions, scattering and interbed multiples.

[23] For a CO<sub>2</sub>-filled layer beneath a thin mudstone layer, the size of the reflection coefficient depends on the thickness of the layer, on its saturation, and on the saturation of overlying and underlying strata. A lower reflection coefficient is generated by reducing the acoustic impedance contrast between a sandstone and its capping mudstone. This reduction can occur in several different ways. First, CO<sub>2</sub> saturation within the sandstone layer can decrease. Secondly, the combined effects of frequency tuning and CO<sub>2</sub> saturation can mimic changes in acoustic impedance. For example, if the dominant wavelength of the seismic signal is much greater than the layer thickness, constructive interference occurs at the tuning frequency, which is controlled by layer thickness [Arts *et al.*, 2004; Chadwick *et al.*, 2005] (Figure 11). Normally, tuning causes reflections to brighten. For source wavelets extracted from the Sleipner seismic data, the tuning thickness is ~9 m. However, if a CO<sub>2</sub> saturated layer thickens to greater than its tuning thickness, the effect of tuning diminishes and reflectivity decreases by up to one third [Chadwick *et al.*, 2005].

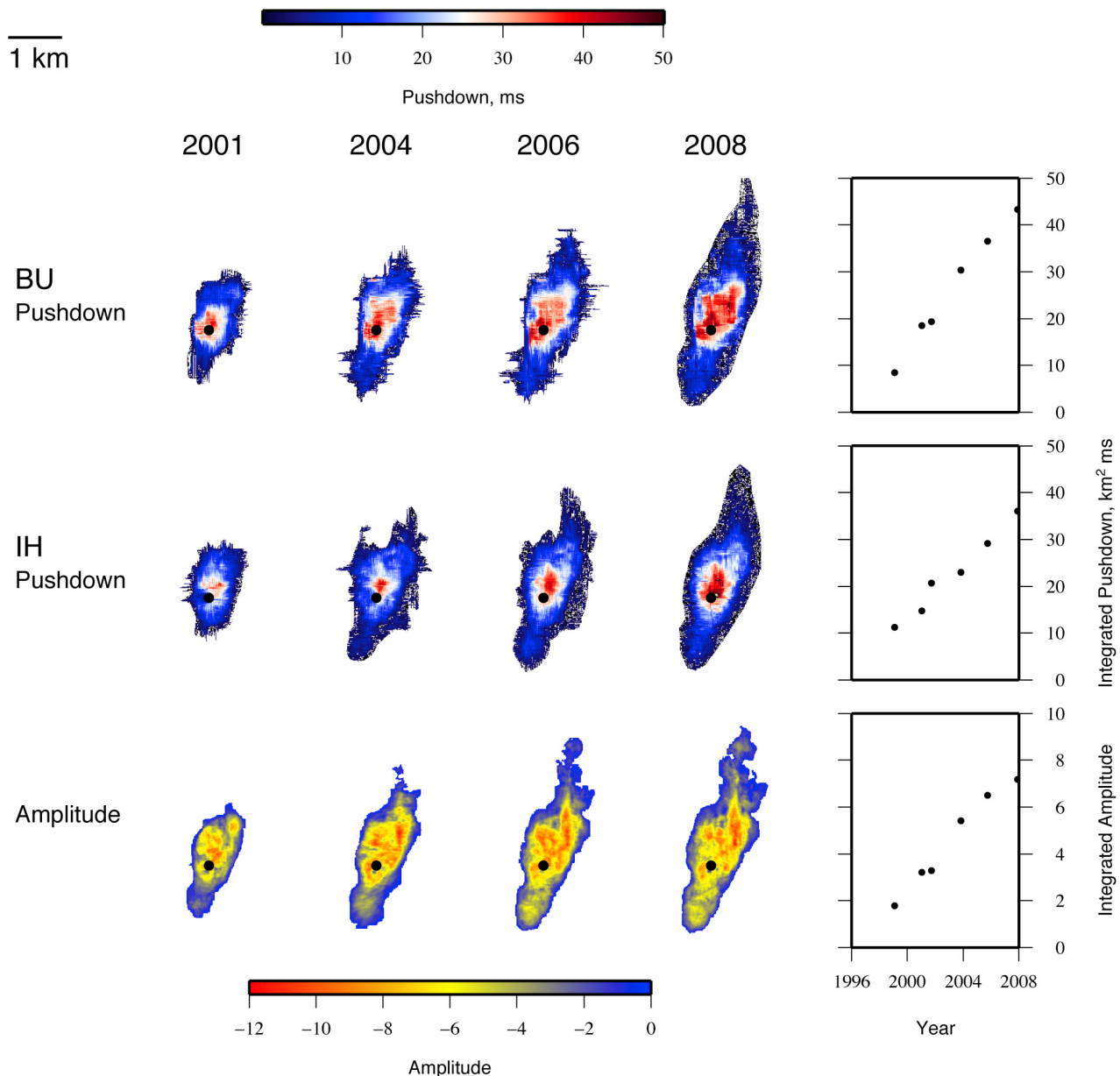


**Figure 7.** Size of pushdown plotted as a function of time for base Utsira (BU) and intraHordland (IH) horizons. (top, middle) Sequence of four pushdown maps for BU and IH; integrated pushdown as a function of time displayed on right-hand side. Pushdown is measured from difference in two-way travel time (ms) between surface mapped on 1994 and subsequent surveys; integrated pushdown is measured by summing pushdown over its lateral extent. Differences between BU and IH are within mapping uncertainties. (bottom) Four maps of cumulative amplitude for all nine horizons as a function of time; integrated cumulative amplitude as a function of time shown on right-hand side.

[24] Thus, disentangling the effects of varying reflection coefficient and signal strength is not straightforward, especially when tuning effects are important. Here, we exploit post-stack amplitude maps of horizons above, within and below the reservoir. Our approach is similar to using normalized root mean squared analysis, which yields the same results. First of all, amplitudes of horizons above and below the reservoir were compared for the 1994, 2001, 2006 and 2008 surveys. Within the reservoir, horizon amplitudes were compared for the 2001, 2006 and 2008 surveys only, since

the internal structure of the reservoir is not adequately resolved on the baseline survey. These particular surveys were chosen because they have comparable amplitudes which were carefully balanced during post-stack processing. This comparability is bolstered by the temporal consistency of stacked and averaged amplitudes for horizons located above the reservoir at travel times of 425 and 650 ms (Figure 9). In this way, the effects of minor acquisitional and processing differences can be discounted. In Figure 10, amplitude transects for horizons below and within the

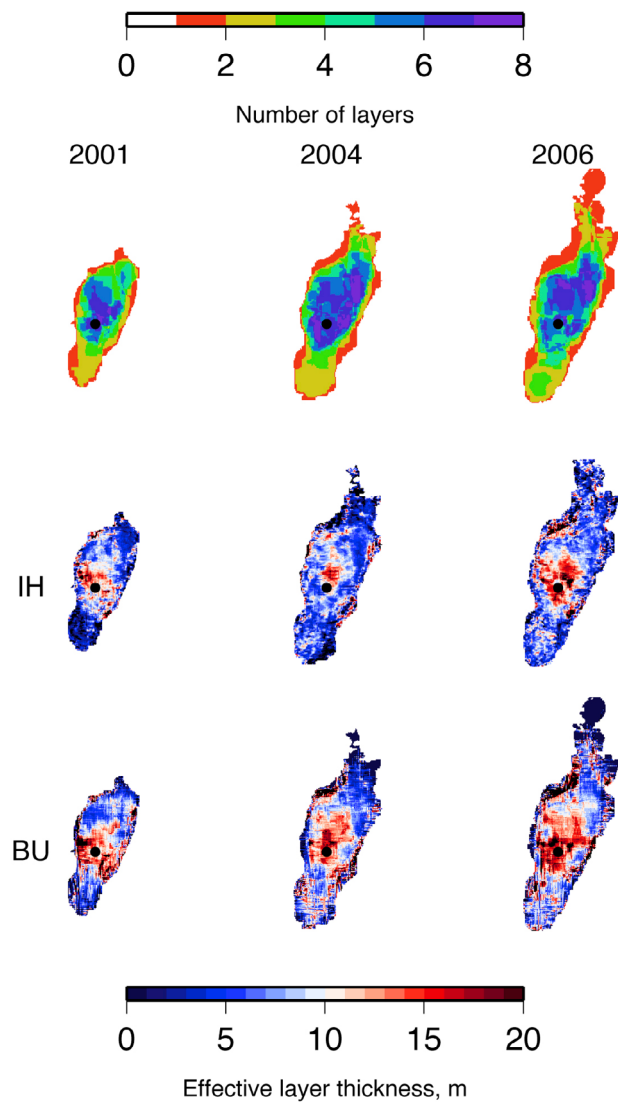


**Figure 8.** Relationship between pushdown and average layer thickness. (top) Contour plots which show number of layers for 2001, 2004 and 2006. (middle) Calculated layer thicknesses for 2001, 2004 and 2006 which were determined by dividing the observed pushdown of IH by the number of layers and correcting for velocity of sandstone, which is homogeneously saturated with  $>30\%$  CO<sub>2</sub> (i.e.  $1428 \text{ m s}^{-1}$ ). (bottom) Calculated layer thicknesses from pushdown of BU.

reservoir are compared for 4 different surveys. This comparison enables us to separate out effects caused by variations in reflection coefficient and in signal strength as a function of time. Although the amplitudes of horizons BU and IH beneath the reservoir were analyzed, only the IH horizon is shown in Figure 10 because it is flat with a uniform amplitude on the baseline survey.

[25] Since the aperture of the seismic experiment is comparable to the depth of the IH horizon and since the sedimentary sequence is sub-horizontal, acoustic energy which reaches the IH horizon travels by sub-vertical incidence through the CO<sub>2</sub> plume. Therefore, changes in the amplitude of IH with time must be caused by changes in acoustic

attenuation, which arise from CO<sub>2</sub> injection. Average amplitude of the BU and IH horizons decreases by more than 50% between 1994 and 2001. Between 2001 and 2008, and especially between 2006 and 2008, there is little change. An obvious exception is the southern end of the IH horizon between 2001 and 2006 where there is a decrease in amplitude of  $\sim 50\%$  (Figure 10b). This local decrease can be attributed to signal loss caused by the lateral spreading of CO<sub>2</sub> within horizons 3, 5 and 7 (Figure 4). The overall lack of change for both BU and IH between 2001 and subsequent surveys implies that continued accumulation of CO<sub>2</sub> does not produce further signal loss. This observation suggests that amplitude dimming within the plume must be at least partly caused by changes in reflection coefficient.

[26] Figure 10 also shows amplitude changes of horizons 1, 5, 8 and 9 for four surveys. The three stages of horizon evolution are evident. Horizons 8 and 9 are at stage one between 2001 and 2006 (i.e. layers grow and brighten). Between 2006 and 2008, these horizons are at stage two, when the central core dims. Horizons 1 and 5 reach stage two at an earlier time (i.e. 2001–2006) and between 2006 and 2008 their amplitudes diminish overall, suggesting that they have now reached stage three. The crucial observation is that amplitude changes of these horizons are far greater than those observed for the BU and IH horizons. For example, between 2001 and 2006 the amplitude of horizon 5 is observed to decrease by up to 40%, while at the same location the amplitude of IH slightly increases. Incontrovertible evidence that all the horizon dimming is not caused by signal attenuation is provided by examining horizon 9 between 2006 and 2008. Since this horizon is at the top of the reservoir, its amplitude decrease cannot be caused by temporal changes of attenuation within the overlying stratigraphic pile. If the thickness of a CO<sub>2</sub>-filled layer exceeds the tuning thickness, the amplitude decreases by  $\sim 1/3$  (Figure 11). Since amplitude dimming is usually greater, we conclude that it is more likely to be caused by a decrease in reflection coefficient, which result from layer-scale changes in CO<sub>2</sub> distribution.

[27] A decrease in amplitude can occur if CO<sub>2</sub> saturation drops below 30%. The relationship between acoustic impedance and saturation closely resembles that between acoustic velocity and saturation [Carcione *et al.*, 2006]. For saturations of less than 30%, acoustic impedance is sensitive to small changes in CO<sub>2</sub> saturation within the brine. If pushdown within the center of the reservoir increases with time, a decrease in both the cumulative amplitude and in the amplitudes of individual horizons can be accounted for in one of two ways. First, CO<sub>2</sub> could migrate into the higher part of the reservoir where the bulk modulus is lower. This migration will cause lower horizons to dim, higher horizons to brighten, and cumulative pushdown to increase. Secondly, low saturations of CO<sub>2</sub> could become distributed between CO<sub>2</sub>-filled layers. Redistribution of CO<sub>2</sub> into the upper parts of the reservoir will cause a net decrease in seismic velocity, given the relationship between acoustic velocity, pressure and temperature [Han *et al.*, 2010]. This velocity decrease amplifies pushdown without altering the total mass of CO<sub>2</sub> in the central part of the reservoir. However, the expected reduction in acoustic velocity between horizon 1 and 9 is no more than about 7%, which will not substantially increase the observed pushdown.

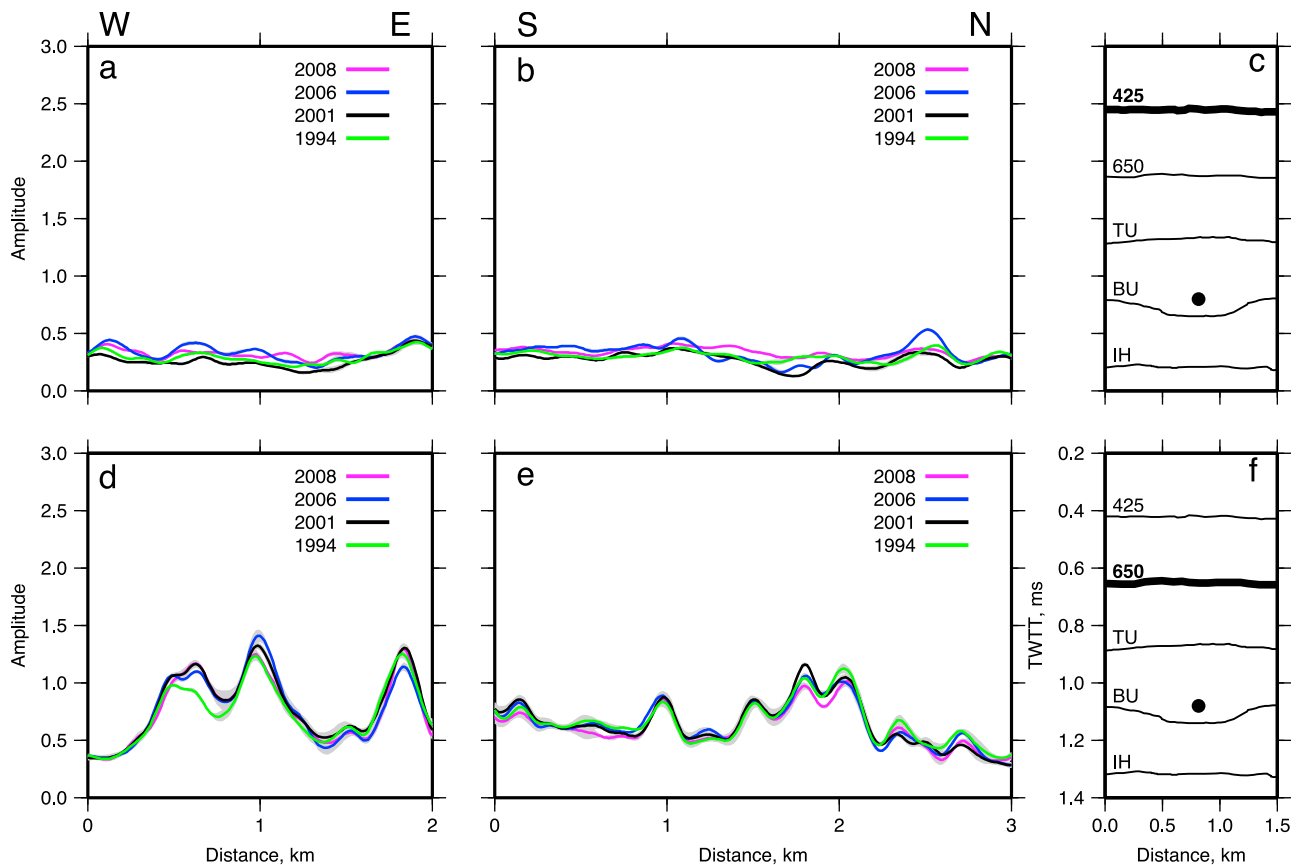


**Figure 9.** Amplitude variation plotted as a function of distance and time for two horizons located above CO<sub>2</sub> plume. In each case, amplitude has been averaged across a 100 m wide corridor, smoothed using a Gaussian function with a width of 300 m, and plotted for 1994 (green), 2001 (black), 2006 (blue), and 2008 (magenta). Gray band = 1  $\sigma$  variation. (a, b) Temporal variation of amplitude in N-S and W-E directions for horizon located 425 ms beneath seabed; (c) location of 425 ms horizon; (d, e) temporal variation of amplitude for horizon located 650 ms beneath seabed; (f) location of 650 ms horizon. Note modest change in amplitude as a function of time.

[28] In summary, small amplitude changes beneath the reservoir between 2001 and 2008 suggest that acoustic energy traveling through the reservoir is not significantly attenuated during this time interval. This observation implies that amplitude dimming and brightening of individual CO<sub>2</sub>-filled horizons are probably caused by layer-scale changes in CO<sub>2</sub> distribution. Since wholesale reduction of CO<sub>2</sub> concentration within the central part of the reservoir cannot account for the observed pushdown, we conclude that some proportion of CO<sub>2</sub> is redistributed between horizons.

#### 4. A Preliminary Layer Growth Model

[29] The seismic images of Figure 4 show that CO<sub>2</sub>-rich horizons spread out as a function of time. In some cases, there is evidence for later retreat or shrinkage. It is generally agreed that ~1 m thick mudstones distributed throughout the reservoir are low permeability barriers which partially trap CO<sub>2</sub> [Zweigel *et al.*, 2001]. However, the way in which dense CO<sub>2</sub> spreads throughout a given layer is not fully understood. In the hydrocarbon industry, numerical reservoir simulation models are generally used to understand the way in which multiphase fluids flow through pipes and rocks. This

approach has been applied with limited success to the Sleipner sequestration experiment [e.g., Chadwick *et al.*, 2009a; Boait *et al.*, 2011]. An alternative, but equally fruitful, approach exploits analytical solutions to fluid dynamical equations.

[30] Bickle *et al.* [2007] model the growth of each layer as an axisymmetric gravity current, which is fed at a point source beneath a horizontal barrier. It is also clear that the way in which CO<sub>2</sub> spreads through a sandstone layer is influenced by topography of the overlying mudstone [Singh *et al.*, 2010]. A number of observations need to be reconciled with the inferred internal structure of the reservoir. These observations include localized linear boundaries repeating in adjacent layers, various linear features within layers, a general tendency to ellipsoidal shapes elongated in a NNE-SSW direction, the prominent spur on horizon 9 and the spur initiated on the 2006 survey of horizon 2. Chadwick and Noy [2010] note that the geometry of the uppermost horizon 9 is largely accounted for by topography on the base of the caprock, which they mapped on the baseline survey. However, the internal structure of the reservoir is poorly imaged on the baseline survey and so other means must be used to assess the importance of intrareservoir topography.

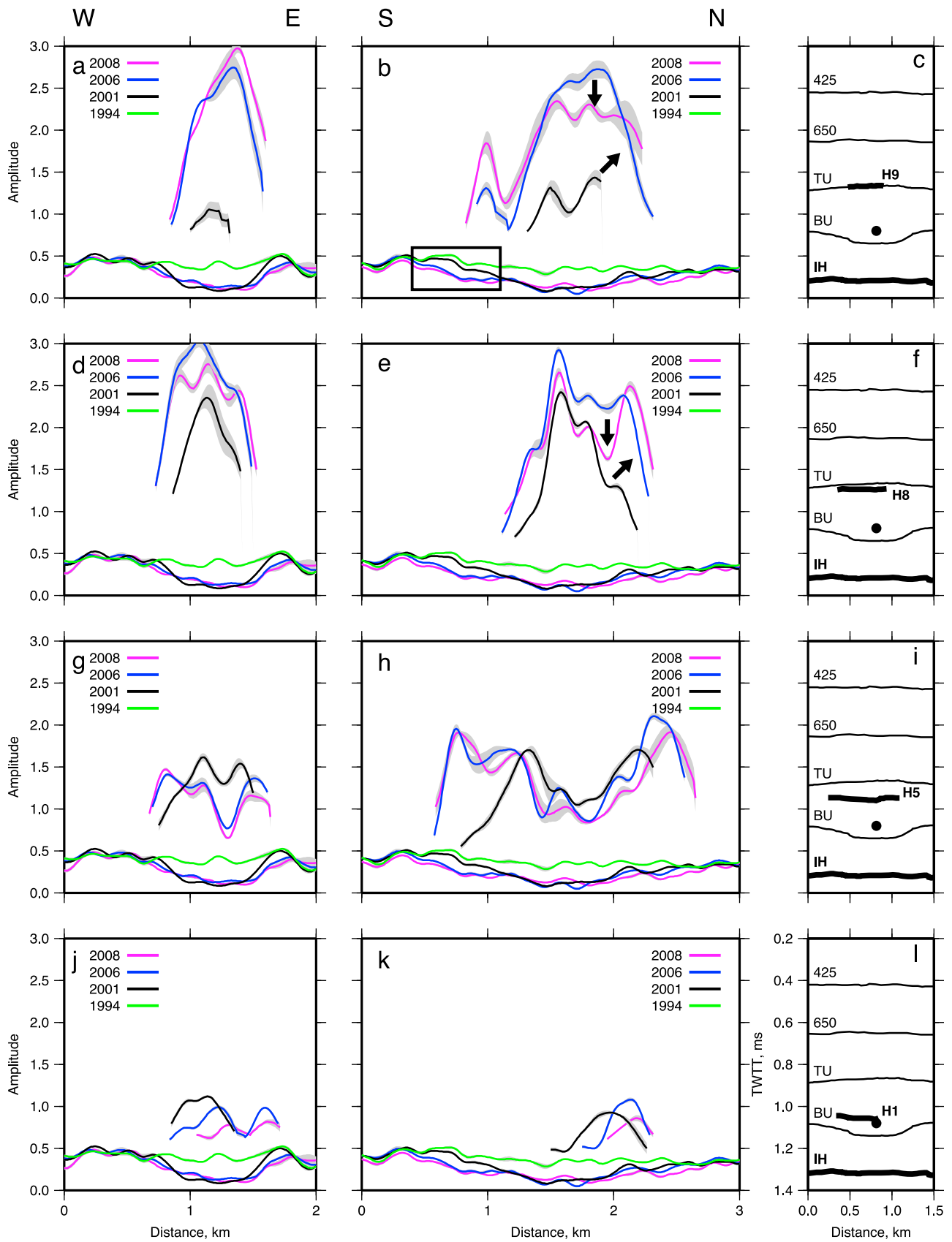
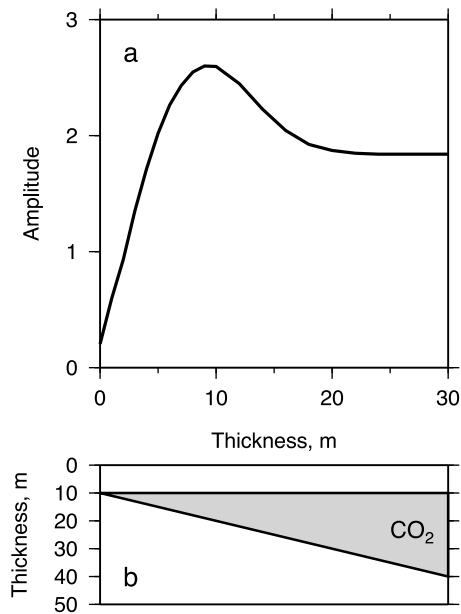


Figure 10



**Figure 11.** (a) Amplitude calculated as a function of thickness of a CO<sub>2</sub>-saturated layer located within brine-saturated sandstone. (b) A cross-sectional sketch showing the increasing thickness of the CO<sub>2</sub>-saturated layer corresponding to the amplitude-thickness curve in Figure 11a. We used proprietary PWTIM reflectivity algorithm of Schlumberger Limited, which assumes a plane wave traveling within a transversely isotropic medium. A 30 Hz zero-phase Ricker wavelet was based upon a source wavelet extracted from seismic data. Maximum amplitude is for a tuning thickness of 9 m.

Here, we exploit the way in which each CO<sub>2</sub>-rich layer has grown to assess the applicability of different spreading models.

#### 4.1. Gravity Currents or Topographic Control?

[31] The way in which a layer of CO<sub>2</sub> spreads outwards depends upon the relative importance of gradients in the hydrostatic pressure within the current that drive flow and of gradients within the bounding topography (Figure 12). During the early stages of layer spreading, it is likely that hydrostatic pressure gradients are greater than topographic gradients. Therefore, the rate of spreading as well as the thickness of current are determined by the input flux, by the time since initiation, by the density contrast, and by the effective permeability of the porous medium [Lyle *et al.*, 2005; Golding *et al.*, 2011] (Appendix A). The influence of topographic gradient will increase with time as hydrostatic gradients diminish. Here, we consider two important end-members: the spreading of a buoyant gravity current along a horizontal surface, and the topographic control arising from flow into a steep-sided hemi-ellipsoidal trap.

[32] Bickle *et al.* [2007] showed that the growth and extent of the Sleipner CO<sub>2</sub> layers are consistent with spreading by gravity currents provided that the effective permeability of the Utsira Sand is  $\sim 2 \times 10^{-13} \text{ m}^2$  (note that temperatures used by Bickle *et al.* [2007] to determine the CO<sub>2</sub> properties are higher than Alnes *et al.* [2011] estimates). Lower temperatures will increase the effective permeability to  $\sim 6 \times 10^{-13} \text{ m}^2$ , which is still considerably smaller than regional permeability measurements for the Utsira formation ( $1\text{--}8 \times 10^{-12} \text{ m}^2$  [Zweigel *et al.*, 2004]). Bickle *et al.* [2007] suggested that the difference is attributable to a reduction in relative permeability caused by two phase flow of CO<sub>2</sub> through brine. However, Golding *et al.* [2011] show that the expected reduction in relative permeability is too small to account for this discrepancy. Dissolution of CO<sub>2</sub> into brine does not resolve this discrepancy since recent calculations suggest that only 10% dissolution occurs, which increases permeability by  $6.5 \times 10^{-13} \text{ m}^2$  [Neufeld *et al.*, 2011a].

[33] A theoretical model, supported by laboratory experiments, indicates that during the propagation of axisymmetric porous gravity currents with constant input flux, the average radius increases with the square root of time. The central thickness remains approximately constant [Lyle *et al.*, 2005]. Bickle *et al.* [2007] exploited acoustic images from the 1999, 2001 and 2002 surveys to argue that layer growth occurred primarily by spreading of a gravity current. Here, their analysis has been extended to other years up to 2008 (Figure 13). It is clear that horizons 5, 6, 8 and 9 have continued to grow with effective radii which are proportional to the square root of time. Horizons 1, 2, 3 and 7 also exhibit a linear relationship until 2004, after which spreading stalls or shrinks, which suggests that vertical migration from layer to layer becomes more important. Horizon 4 starts to shrink between 2001 and 2002. Our confidence in the use of these plots to identify horizons dominated by gravity flow is limited given that the shape of possible topographic traps is largely unconstrained. For example, filling of hemispherical channels also show a linear increase of area with time [Golding and Huppert, 2010]. If the impermeable cap has a significant slope, the current will initially spread as a circular flow and later spread elliptically [Vella and Huppert, 2006]. However, the parameters in Table 2 and a maximum slope of  $1.2^\circ$  suggest that the minimum timescale for this transition is  $O(10)$  years [Vella and Huppert, 2006].

[34] The eccentric planforms of horizons 5 and 7 are almost constant through time, which suggests that these horizons have not grown on an inclined plane (Figure 5). Instead, domal traps which approximate to hemi-ellipsoidal surfaces are more plausible. The filling of an inverted hemi-ellipsoidal trap can be expressed as a relationship between area (i.e. radius squared) and time (Appendix A). For given values of the principal axes (i.e.  $a, b, c$ ), the input flux,  $Q$ , can be varied to fit the growth pattern of the nine horizons

**Figure 10.** Amplitude variation plotted as a function of distance and time for four horizons within, and 1 horizon below, CO<sub>2</sub> plume (see Figure 9). (a–c) Variation of amplitude in N-S and W-E directions for Horizon 9 (H9) located just beneath top of Utsira Formation (TU); (d–f) variation for Horizon 8 (H8) located close to top of reservoir; (g–i) variation for Horizon 5 (H5) located in middle of reservoir; (j–l) variation for Horizon 1 (H1) at base of reservoir near injection point. In each case, amplitude variation also shown for intraHordalandformation (IH) beneath reservoir. Amplitude changes within reservoir are larger than those beneath (solid arrows). Box in Figure 10b highlights minor decrease for IH from 2001 to 2006 when CO<sub>2</sub> extends southward.

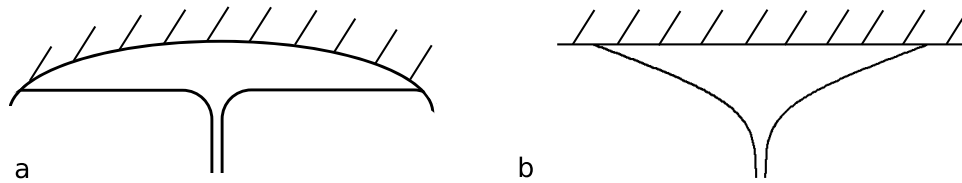


**Figure 12.** Sketches which illustrate differences between (a) spreading of a gravity current along a horizontal interface, and (b) topographic control of spreading beneath an ellipsoidal trap.

(Figure 14). Filling of hemi-ellipsoidal traps yields much poorer fits compared with the spreading of a gravity current over a horizontal surface (see residual misfit values on Figures 13 and 14). Furthermore, the required input fluxes are up to one order of magnitude greater than expected. For a

given permeability, the predicted gradients of gravity flows are greatest at the onset of spreading and decrease with time. This observation suggests that flow is controlled by hydrostatic pressure gradients at earlier times with increasing topographic influence at later times (Figure 15).

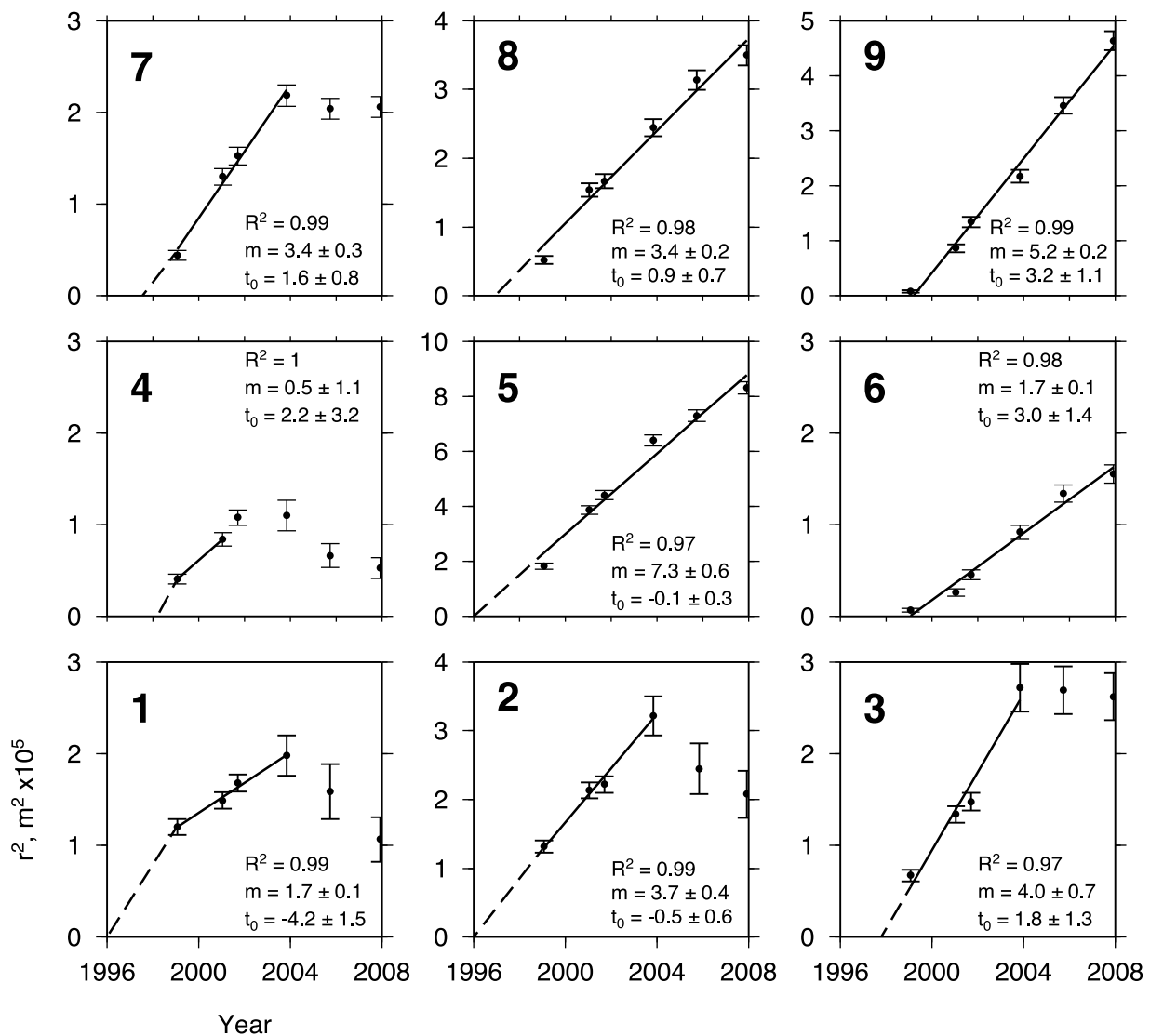


**Figure 13.** Square of horizon radii plotted as a function of time elapsed since start of injection for all nine mapped horizons (Figure 4). Solid circles and error bars show measured values and their uncertainties; solid lines show best-fit lines; dashed lines show extrapolation of best-fit lines. Coefficients of determination,  $R^2$ , slopes,  $m$ , and intercepts at zero radius,  $t_0$ , are shown. Input flux,  $Q$ , for horizons 1–9 are 0.0006, 0.003, 0.004, 0.001, 0.01, 0.0007, 0.003, 0.002, and 0.007. Note departure of last two or more data points from radius-squared relationship for horizons 1, 2, 3, 4 and 7.

**Table 2.** Parameter Values and Definitions<sup>a</sup>

Symbol	Parameter	Value
$\phi$	Utsira sst porosity	0.27 – 0.41
	Utsira sst permeability	$1 - 3 \times 10^{-12} \text{ m}^2$
	Caprock permeability	$4 \times 10^{-19} \text{ m}^2$
$b$	typical mudstone thickness	1 m
$\mu_n$	viscosity CO <sub>2</sub>	$5.37 - 5.60 \times 10^{-5} \text{ Pa s}$
$\rho_n$	density CO <sub>2</sub>	$683 - 701 \text{ kg m}^{-3}$
$\mu_w$	viscosity water	$7 \times 10^{-4} \text{ Pa s}$
$\rho_w$	density water	$1020 \text{ kg m}^{-3}$
$L_c$	critical length	~50 cm
$K$	bulk modulus of brine	2.3 GPa
$f$	frequency of seismic source	30 Hz
$r_N$	radius	m
$t$	time	s
$h$	height of current	
$Q$	input flux	$0.04 \text{ m}^3 \text{ s}^{-1}$
$u_b$	buoyancy velocity	$4.3 \times 10^{-6} \text{ m s}^{-1}$
$M$	mobility ratio	13
$h_c$	capillary entry height	$1. \times 10^{-20} \text{ m}$
$k$	sandstone permeability	$7.5 \times 10^{-14} \text{ m}^{2*}$
$k_b$	mudstone permeability	$1.15 \times 10^{-16} \text{ m}^{2*}$
$g$	gravitational acceleration	$9.81 \text{ m s}^{-2}$
$\Delta\rho$	$\rho_w - \rho_n$	$319 \text{ kg m}^{-2}$
$\alpha$	controls rate of flux released	1
$\eta_N$	similarity variable	1.15
$p$	pressure	Pa
$z$	depth	m
$l$	height within mudstone	m
$w_n$	vertical velocity brine	$\text{m s}^{-1}$
$w_n$	vertical velocity CO <sub>2</sub>	$\text{m s}^{-1}$
$\lambda_w$	mobility of brine	$\text{m}^2 \text{ Pa}^{-1} \text{ s}^{-1}$
$\lambda_n$	mobility of CO <sub>2</sub>	$\text{m}^2 \text{ Pa}^{-1} \text{ s}^{-1}$
$R$	non-dimensional radius	
$T$	non-dimensional time	
$H$	non-dimensional height	

<sup>a</sup>In Figure 16, parameters marked \* were varied to fit observations.

[35] Gravity currents have a constant central thickness but the central thickness obtained by filling a hemi-ellipsoidal trap should increase as a function of areal extent (Appendix A). Simple estimates of central thickness variation can be made from seismic images by assuming that the radial variation of amplitude for a given CO<sub>2</sub>-filled layer is primarily controlled by layer thickness [Arts *et al.*, 2004; Bickle *et al.*, 2007]. In the 1999, 2001 and 2002 surveys, CO<sub>2</sub>-filled layers are thin and amplitude is roughly proportional to thickness [Arts *et al.*, 2004] (Figures 4 and 11). Bickle *et al.* [2007] show that for these particular surveys, central thicknesses remain approximately constant for horizons 6, 8 and 9 and are therefore more consistent with spreading by gravity currents.

[36] Figure 15 shows how the distal slope of the free surface of a gravity current spreading on a flat surface varies as a function of time for a range of permeabilities. This calculation assumes that the input flux,  $Q = 0.04 \text{ m}^3 \text{ s}^{-1}$ , the buoyancy velocity,  $u_b = 4.3 \times 10^{-6} \text{ m s}^{-1}$ , and the porosity,  $\phi = 0.37$  (Table 2). Initial slopes are  $\sim 1.6^\circ$  for all permeabilities, which is greater than slopes estimated by seismic mapping. Within the reservoir, slopes are easily estimated on the baseline survey from the shape of the base of the capping mudstone. Along the base of the Nordland Shale, slopes range from  $0.006^\circ$  in a north-south direction along the long axis of the culmination to a maximum of  $1^\circ$  across the main central dome [Chadwick *et al.*, 2009a; Chadwick and Noy, 2010]. Combined with the existence of eccentric planforms, these values suggest that topographic influence is not completely negligible.

## 4.2. Layer Initiation Times

[37] If CO<sub>2</sub> spreads as a gravity current, the horizontal intercepts on Figure 13 represent initiation times of spreading. In the case of horizon 1, this inference implies that the amount of trapped CO<sub>2</sub> has decreased over time. Initiation times of horizons 2, 5 and 8 are the same (i.e. 1996), which agrees within error with the initiation of injection. In contrast, a spreading model shows that horizons 3, 6, 7 and 9 initiated 1.8, 3, 1.6 and 3.2 years after the start of injection. These delays are consistent with two permeable pathways by which CO<sub>2</sub> rises through the reservoir. The first pathway is more permeable and CO<sub>2</sub> rapidly reaches the highest levels of the reservoir: CO<sub>2</sub> should rise at 40 m/day through a connected CO<sub>2</sub>-rich column within sandstone, which has a permeability of  $2 \times 10^{-12} \text{ m}^2$ . The second pathway is one in which CO<sub>2</sub> flow is delayed, either by the time required to penetrate less permeable barriers, or by the time taken for accumulations to spread horizontally to permeable sites within these barriers.

[38] Alternatively, if layer geometry is controlled by hemi-ellipsoidal caps, horizon 1 initiates at the start of injection, horizon 2 after 2.4 years and horizons 3–9 after 3 years (Figure 14). Once again, the implied ascent rate through at least part of the reservoir (i.e. horizons 2–9) is very rapid and the movement of CO<sub>2</sub> from horizons 1 and 2 is delayed by 2–3 years. Wireline logs show that horizon 8 is capped by a 5m thick mudstone and so it is more likely that there would be a delay between the initiation of horizons 8 and 9 (Figure 13).

[39] A further complication concerns the exact location of each point source. The different locus of each layer in the 1999 survey suggests that several independent rising plumes of CO<sub>2</sub> may exist [Chadwick *et al.*, 2005] (Figure 4). Furthermore, the positions of the thickest portions of larger accumulations also implies that layers might be separately fed. Initiation times and loci suggest that different sources feed multiple adjacent layers and that different layers grow from several distinctive locations (e.g. horizons 4, 5, 9).

[40] Together, the initiation times of horizons 2–9, the irregular distribution of initiation points across the reservoir, and the shrinkage of the lower horizons constrain mechanisms by which CO<sub>2</sub> migrates through the reservoir. These mechanisms have a bearing on CO<sub>2</sub> retention within the reservoir. If the thicknesses of CO<sub>2</sub> horizons are primarily controlled by the topography of thin mudstones and if CO<sub>2</sub> migrates upwards through the mudstone where each CO<sub>2</sub> layer is thickest so that capillary entry pressures can be overcome, then a correlation between initiating points of the overlying horizons and thicker portions of the underlying horizons is expected. This correlation is not observed, although it is possible that different initiation points represent accumulations of CO<sub>2</sub>, which have flowed horizontally under the mudstone trap into topographic highs.

[41] Different mechanisms may govern transport of CO<sub>2</sub> through the mudstones and give rise to the observed planforms of Figure 4. Vertical migration through thin mudstone layers may be dominated by a small number of localized, highly permeable pathways (i.e. fractures). However, while localized pathways can explain horizon initiation times, they would lead to a reduction in horizon growth rate [Neufeld *et al.*, 2011b]. It is more difficult to explain the constant or diminishing planforms visible in Figure 13. Several different possibilities are envisaged. First, CO<sub>2</sub> spreads laterally under

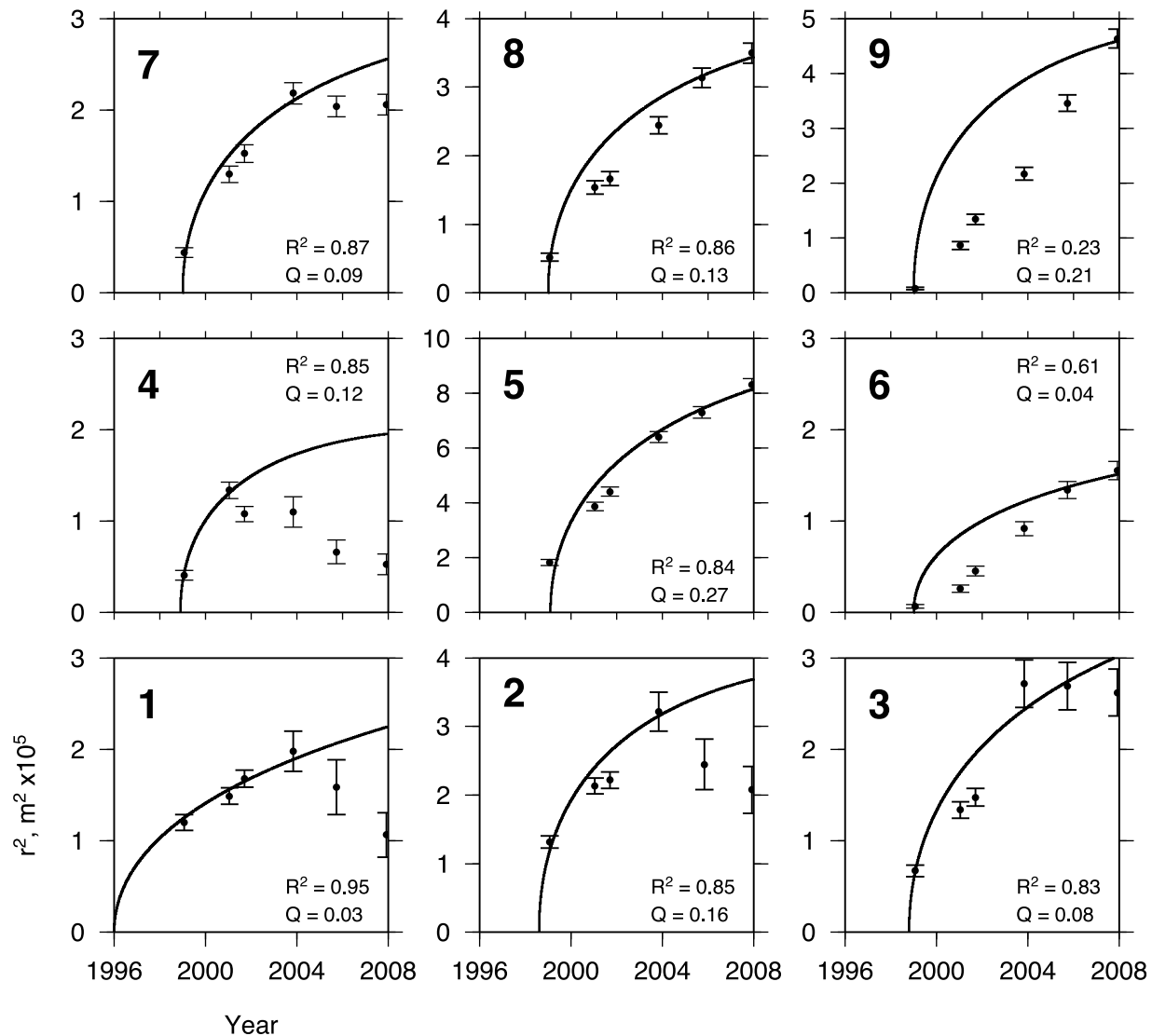


**Figure 14.** Square of horizon radii plotted as a function of time and fitted with model based upon hemi-ellipsoidal trap geometry (Appendix A). Coefficients of determination,  $R^2$ , and input fluxes,  $Q$ , are shown. In each case, input flux,  $Q$  ( $\text{m}^3 \text{s}^{-1}$ ), initiation time,  $a$  and  $b$  have been estimated by fitting observed values.

a mudstone cap until it encounters a path through the mudstone (e.g. fracture, seepage point). If the conductivity of the pathway is large enough, layer growth may cease without causing the layer planform to shrink, provided that the input flux is constant. If flux through the pathway is smaller than the input flux, the layer will continue to grow [Neufeld *et al.*, 2011b]. Secondly, the finite entry pressure of CO<sub>2</sub> into mudstone could permit CO<sub>2</sub> to accumulate until a time when some critical thickness is exceeded. After this time, CO<sub>2</sub> drains upward at a rate controlled by the mudstone's permeability (e.g. Figure 16). Thirdly, as CO<sub>2</sub> penetrates through a mudstone barrier, the flow established above the barrier will tend to pull fluid upward at an increasing rate [Neufeld and Huppert, 2009]. Finally, CO<sub>2</sub> penetration of mudstones could be retarded by the entry pressure and by the pressure gradient required to expel the more viscous brine (Table 2). This delay would be followed by a faster escape of CO<sub>2</sub> once it has saturated the mudstone, and may explain the

initial advance and ultimate retreat of layers 1–4 (see Figures 13 and 16 and Appendix B)

[42] For CO<sub>2</sub> to flow through mudstones at a rate which is significant relative to the duration of the injection experiment, the effective permeability must be greater than  $\sim 10^{-17} \text{ m}^2$ , two orders of magnitude higher than that measured for the overlying Nordland Shale, which acts as the regional seal (Table 2) [Chadwick *et al.*, 2009a]. This conclusion was also drawn by Singh *et al.* [2010], who speculated that flow occurs through micro-cracks. The parameter range for which CO<sub>2</sub> accumulations grow, and then shrink, due to the rising CO<sub>2</sub> plume above the mudstone requires mudstone permeabilities, which are within one order of magnitude of those expected for sandstones. Such highly permeable mudstones would be unable to trap layers of the observed size [Neufeld and Huppert, 2009]. Finite entry pressures might limit layer thickness but should not cause layer shrinkage.

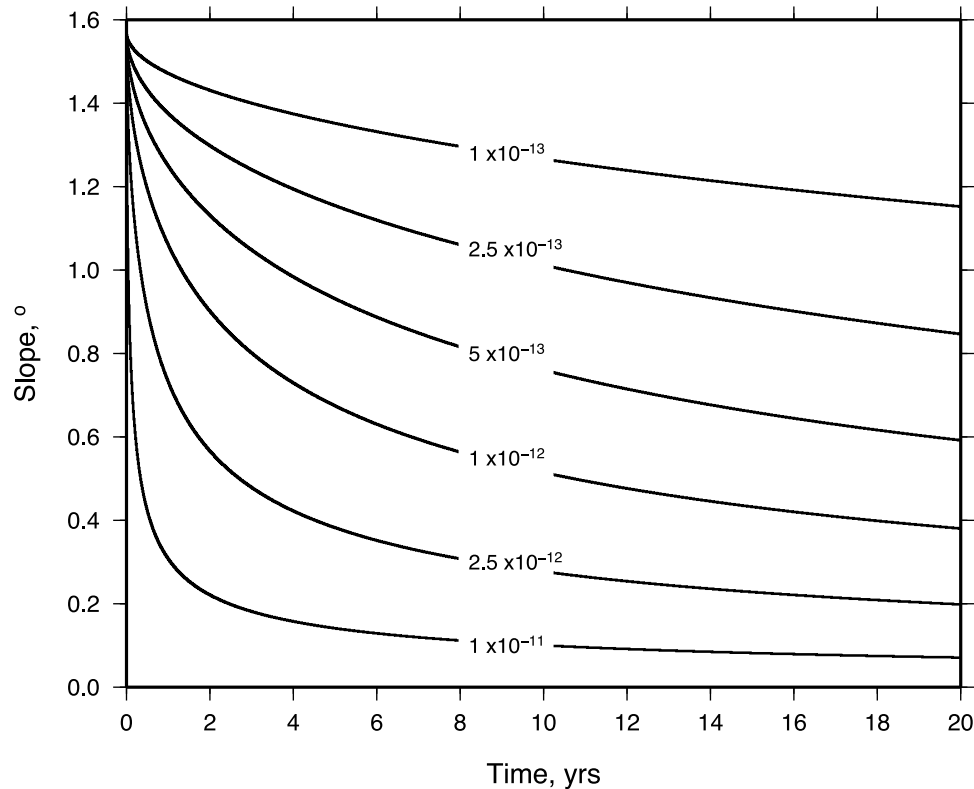


**Figure 15.** Slope in degrees of free surface for a gravity current which spreads on a flat surface plotted as a function of time for range of permeabilities. In each case,  $\phi = 0.37$ ,  $Q = 0.04 \text{ m}^3 \text{ s}^{-1}$ , and  $u_b = 4.3 \times 10^{-6} \text{ m s}^{-1}$  (Table 2). Higher permeability gives rise to more rapid changes in slope.

### 4.3. Vertical Migration

[43] Two phenomena act to retard the rate of CO<sub>2</sub> penetration through thin mudstone layers. First, the magnitude of breakthrough pressures for initial entry of CO<sub>2</sub> into mudstones and secondly the slowing of ascent rate as higher viscosity brine is expelled from the mudstone layer. The behavior of a CO<sub>2</sub> accumulation with a breakthrough, pressure-modulated migration through a capping low permeability horizon can be modeled by modifying the equations describing flow of a low density gravity current in a permeable medium under an impermeable horizontal barrier [Lyle *et al.*, 2005].

[44] Buoyancy-driven flow in the sandstone is assumed to be unconfined because current heights are significantly less than inter-mudstone thicknesses ( $\sim 30 \text{ m}$ ): a typical CO<sub>2</sub>-filled horizon has a maximum height of  $\sim 15 \text{ m}$  and a lateral extent of 1–3 km. Within a sandstone, we assume that the flow of CO<sub>2</sub> can be modeled using an effective viscosity, which reflects a single effective relative permeability. Migration of CO<sub>2</sub> into the overlying mudstone is determined by its vertical velocity; the fluid dynamics of this migration contributes to the long-term behavior of the currents (Appendix B).

[45] Migration through the mudstone layer is driven by the hydrostatic pressure of CO<sub>2</sub>. Over time, the amount of CO<sub>2</sub> within the mudstone layer increases. Pressure gradients drive water out of the mudstone layer, and are important because at low permeabilities pressure at the base of the mudstone can reasonably be assumed to be hydrostatic. Horizontal

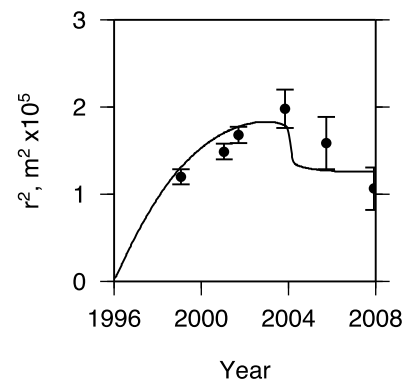


**Figure 16.** Square of horizon radii plotted as a function of time elapsed since start of injection for Horizon 1 (see Figure 4). Solid circles and error bars show measured values and their uncertainties; solid curve shows predicted variation of radius squared as a function of time, which assumes: (1) a source of constant flux; (2) migration through mudstone layer is driven by hydrostatic pressure of CO<sub>2</sub>; (3) hydrostatic pressure at base of mudstone; (4) horizontal velocities within mudstone are negligible and so vertical velocities and pressure gradients do not vary with height; (5) interface between the two fluids is sharp and not caused by variation in saturation.

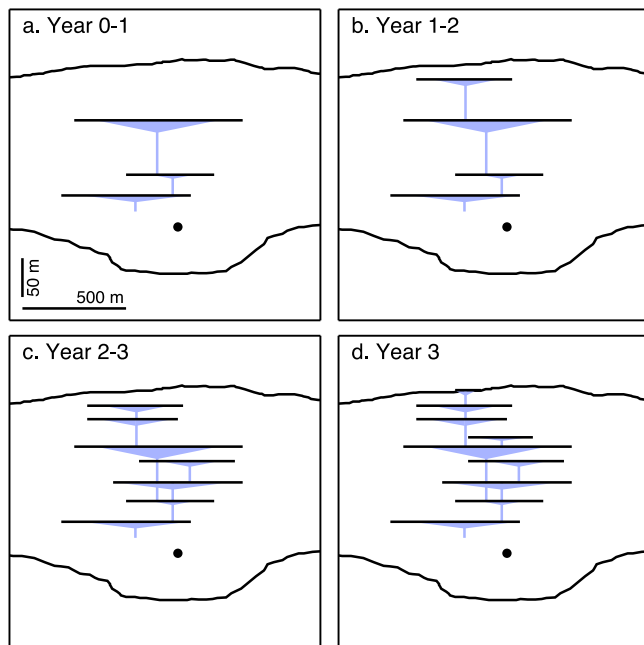


**Figure 17.** Sketches which show evolving geometry of injected CO<sub>2</sub> plume determined from our mapping and analysis. (a) Horizons 1, 2 and 5 begin to accumulate from start of injection; (b) horizon 8 begins to accumulate by end of year 1; (c) horizons 3, 4 and 7 begin to accumulate within 2 years; (d) horizons 6 and 9 begin to accumulate within 3 years.

velocities within the shale layers are small and can be neglected so that vertical velocities and pressure gradients do not vary with height.

[46] The scaling of time and horizontal distance depends on three poorly constrained parameters: the effective multiphase permeabilities of the sandstone and of the mudstone,  $k$ , and  $k_b$ , and the input flux,  $Q$ , which is assumed to be constant. Without reliable CO<sub>2</sub> layer thicknesses, only two of these parameters can be constrained. Figure 16 shows how the growth and shrinkage of horizon 1 can be matched by varying  $k$  and  $k_b$  (Table 2). This model predicts growth at a decreasing rate followed by abrupt shrinkage to a steady state condition. The gradual change contrasts with the markedly saw-shaped profile of horizons which exhibit shrinkage. The vertical velocity depends on the difference between the viscosity of CO<sub>2</sub> and brine, as well as on the thickness of the mudstone, the buoyancy velocity, and the permeabilities of both sandstone and mudstone.

## 5. Discussion

[47] The key issue is whether the observed dimming of lower horizons is an artefact of seismic imaging, or whether it is real and caused by penetration of CO<sub>2</sub> into the impermeable mudstones. Partial CO<sub>2</sub> saturation of brine between CO<sub>2</sub> horizons both increases pushdown and diminishes horizon amplitude by reducing the acoustic impedance contrast between sandstone and mudstone layers. There is some evidence that a proportion of CO<sub>2</sub> rises rapidly through the reservoir along relatively high permeability conduits [Chadwick and Noy, 2010]. For example, CO<sub>2</sub> reaches horizon 9 in sufficient quantities to be observed, within

3 years. The rest of the injected CO<sub>2</sub> takes substantially longer, presumably delayed by the time taken for CO<sub>2</sub> to saturate thin mudstones which have lower permeabilities. If CO<sub>2</sub> eventually penetrates the thin mudstones, small distributed fluxes of CO<sub>2</sub> might then cause partial saturation of brines beneath the overlying CO<sub>2</sub>-rich horizons. The effect of the distributed, low-saturation CO<sub>2</sub>, would be potentially enhanced by the markedly non-linear variation of seismic velocity and reflection coefficients with homogeneous CO<sub>2</sub> saturation, but the distribution of saturation is uncertain. The critical length for patchy saturation is given by the distance,  $L_c$ , over which pore pressures equilibrate at seismic frequencies where

$$L_c \approx \sqrt{\frac{kK}{\mu f}}. \quad (1)$$

Here  $k$  is the permeability,  $K$  is the bulk modulus of the brine,  $\mu$  is viscosity of the brine, and  $f$  is the frequency of the seismic source. If  $f = 30$  Hz and if other parameter values are chosen to be appropriate to this injection experiment,  $L_c$  is  $\sim 50$  cm [Mavko and Mukerji, 1998] (Table 2). Thicknesses of sandstone beds are of this order and since low viscosity CO<sub>2</sub> is expected to exhibit viscous fingering, saturation is probably patchy. If so, seismic velocities and impedance will exhibit a more linear variation with saturation [Mavko and Mukerji, 1998]. However, the existence of bright reflections indicates that layers with high saturation exist. Although precise thicknesses, saturations and distributions of CO<sub>2</sub>-filled layers are poorly known, it is clear that the reservoir as a whole does not have uniform saturation since time-varying reflectivity is observed. It is likely that the distribution of CO<sub>2</sub> tends toward a homogeneous end-member in which highly saturated layers occur with patchy saturation elsewhere. High resolution seismic experiments could be designed to shed light on these predicted distributions.

## 6. Conclusions

[48] We have mapped and analyzed the growing accumulation of injected CO<sub>2</sub> within a saline reservoir close to the Sleipner field in the North Sea. Pushdown measurements of reflections below the plume show that the mass of CO<sub>2</sub> is increasing in the central part of the plume. This increase contrasts with the reflectivity of several CO<sub>2</sub>-filled horizons whose centers have significantly dimmed. The highest horizon starts to dim in 2008 while those located below the plume do not continue to dim. Both observations, coupled with analysis of post-stack amplitudes, suggest that a primary cause of intraplume dimming is layer-scale changes of CO<sub>2</sub> distribution. These acoustic impedance changes probably arise from a combination of tuning effects and the growth of inter-layer CO<sub>2</sub>. Pushdown modeling suggests that some CO<sub>2</sub> is present between the well-imaged, higher saturation CO<sub>2</sub> layers. Figure 17 summarizes the evolving geometry of the CO<sub>2</sub> accumulation. No leakage model can be regarded as definitive because mechanisms by which CO<sub>2</sub> penetrates impermeable mudstone layers are still poorly understood.

[49] The density of CO<sub>2</sub> together with the effective porosity and permeabilities of both the Utsira Sand and the interbedded mudstones are key parameters for successful modeling of CO<sub>2</sub> accumulation. In spite of these large

uncertainties, we have shown that a combination of areal growth plots, pushdown calculation and amplitude analysis provides a valuable set of constraints. Initiation times, growth characteristics and predicted permeabilities suggest that flows are primarily controlled by the spreading of gravity currents whose planforms are moderated by topographic infilling.

## Appendix A

### A1. Gravity Spreading

[50] Axisymmetric spreading of a buoyant plume of CO<sub>2</sub> within a porous medium, which is bounded by an impermeable, and horizontal, cap rock is described in detail by *Lyle et al.* [2005]. These authors showed that for a constant input flux,  $Q$ , the current rapidly assumes a self-similar profile whose radial extent is given by

$$r_N(t) = 1.15 \left( \frac{u_b Q}{\phi^2} \right)^{\frac{1}{2}} t^{\frac{1}{2}}, \quad (\text{A1})$$

where  $\phi$  is the porosity of the rock matrix,

$$u_b = \frac{\Delta \rho k g}{\mu_n} \quad (\text{A2})$$

is the buoyancy velocity,  $\Delta \rho$  is the density difference between CO<sub>2</sub> and ambient brine within the aquifer,  $k$  is the permeability of the Utsira sandstone,  $g$  the gravitational acceleration, and  $\mu_n$  the viscosity of CO<sub>2</sub> at reservoir temperatures and pressures (Table 2). Note that equation (A1) is the corrected version from *Bickle et al.* [2007].

### A2. Filling Topography

[51] We assume that the topography of a mudstone cap approximates an inverted hemi-ellipsoid with principal axes  $a$ ,  $b$  and  $c$  ( $a$  and  $b$  are the horizontal axes, where  $b > a$ , and  $c$  is the vertical axis). If this hemi-ellipsoid is filled with fluid, the horizontal area of fluid at a height  $z$ ,  $A(z)$ , is given by

$$A(z) = \pi ab [(2z/c) - (z^2/c^2)], \quad (\text{A3})$$

where  $z$  is the thickness of the fluid layer in the center of the hemi-ellipsoid. The volume of fluid,  $V(z)$ , is given by

$$V(z) = \pi ab [(z^2/c) - (z^3/3c^2)]. \quad (\text{A4})$$

If the flux,  $Q$ , is constant then

$$t = \frac{\pi ab}{Q c^2} [c z^2 - z^3/3]. \quad (\text{A5})$$

The spreading radius,  $r(t)$ , is given by

$$t = \frac{\pi abc}{Q} [R^2 - R^3/3], \quad (\text{A6})$$

where

$$R = 1 - \sqrt{1 - r^2/ab}. \quad (\text{A7})$$

## Appendix B

[52] A key feature of the Sleipner seismic data is the pronounced vertical migration through thin mudstones. Models of buoyancy-driven propagation along an impermeable, horizontal cap rock cannot model the longer term dynamic evolution whereby loss through thin layers of mudstone becomes important. Instead, the three stages of advance, saturation and retreat exhibited by the areal extents of the lowermost layers require a model of drainage through the intervening mudstone layers. Here, we derive a drainage law which models leakage of CO<sub>2</sub> through a brine-saturated mudstone layer.

[53] Spreading of buoyant CO<sub>2</sub> along a horizontal shale layer and its subsequent leakage through a thin mudstone is modeled using an extension of the approach of *Lyle et al.* [2005] and *Pritchard et al.* [2001]. They both assume that flow is unconfined and that the velocity of the ambient brine can be neglected. The height,  $h(r, t)$ , of an axisymmetric, buoyant current as a function of its radius,  $r$ , and time,  $t$ , is described by the porous gravity-current equation

$$\phi \frac{\partial h}{\partial t} - \frac{u_b}{r} \frac{\partial}{\partial r} \left( r h \frac{\partial h}{\partial r} \right) = w_s, \quad (\text{B1})$$

where  $w_s$  represents the leakage velocity, or vertical migration, of CO<sub>2</sub> into the overlying confining mudstone layer. The physics of this migration gives rise to the long-term behavior of a current. For simplicity, we model horizon 1, where the source is a known constant input flux,  $Q$ , into the layer at  $r = 0$ . The boundary conditions (i.e. constant input flux at origin) are given by

$$-\left[ 2\pi r u_b h \frac{\partial h}{\partial r} \right]_{r \rightarrow 0} = Q \quad (\text{B2})$$

$$h(r_N) = 0, \quad (\text{B3})$$

where  $r_N$  is the radial extent of the current. Vertical migration of CO<sub>2</sub> through the overlying mudstone, which extends from  $z = [0, b]$ , is driven by the hydrostatic pressure of CO<sub>2</sub> ponded at the base of the mudstone:

$$p(z = 0) = \Delta \rho g h.$$

When buoyant CO<sub>2</sub> invades a mudstone, it must expel the more viscous water. By modeling the fluid interface as sharp and by neglecting horizontal velocities within the mudstone, we find that the vertical fluid velocities of CO<sub>2</sub> and water are

$$w_n = -\lambda_n \left( \frac{\Delta \rho g h - p_i}{l} + \Delta \rho g \right) \quad (\text{B4})$$

$$w_w = -\lambda_w \left( \frac{p_i}{b - l} \right), \quad (\text{B5})$$

where  $p_i$  is the interfacial pressure between water and CO<sub>2</sub> at depth  $z = -l$  and  $\lambda_w = k_b/\mu_w$  and  $\lambda_n = k_b/\mu_n$  are the mobilities of the wetting and non-wetting phases, respectively. Pressure at the base of the mudstone is assumed to be hydrostatic

$p(z = -b) = 0$ . Matching these velocities at  $z = -l$  we solve for pressure and find that the migration velocity is

$$\begin{aligned} w_s = w_n &= -\lambda_n \Delta \rho g \left(1 + \frac{h}{l}\right) \left[ \frac{\lambda_w/b - l}{\lambda_n/l + \lambda_w/b - l} \right] \\ &= -u_b \frac{k_b}{k} \left[1 + \frac{h}{l}\right] \left[1 + M(b-l)/l\right]^{-1}, \end{aligned} \quad (\text{B6})$$

where  $M = \lambda_n/\lambda_w = \mu_w/\mu_n$  is the mobility ratio which, for the sharp interface approximation used here, is equivalent to the ratio of viscosities.

[54] Equations (B1), (B3) and (B6) can be made non-dimensional with vertical, radial and temporal scales so that

$$H = \sqrt{q/\phi u_b} \simeq 20 \text{ m} \quad (\text{B7})$$

$$R = H\sqrt{k/k_b} \simeq 2 \text{ km} \quad (\text{B8})$$

$$T = \frac{k}{k_b} \sqrt{\frac{\phi q}{u_b^3}} \simeq 50 \text{ years}, \quad (\text{B9})$$

where  $u_b = 4.3 \times 10^{-6} \text{ m s}^{-1}$ .

[55] The non-dimensional equations governing flow now become

$$\frac{\partial h}{\partial t} - \frac{1}{r} \frac{\partial}{\partial r} \left( r h \frac{\partial h}{\partial r} \right) = \begin{cases} -\left(1 + \frac{h}{l}\right) \left[1 + M(b-l)/l\right]^{-1} & (l < b) \\ -\left(1 + \frac{h}{b}\right) & (l \geq b) \end{cases} \quad (\text{B10})$$

$$-\left[2\pi r h \frac{\partial h}{\partial r}\right]_{r \rightarrow 0} = 1. \quad (\text{B11})$$

[56] For parameters given in Table 2, we obtain a relationship between the areal extent of horizon 1 and time (Figure 16).

[57] **Acknowledgments.** F.C.B. is supported by the University of Cambridge and by the British Geological Survey. J.A.N. was supported by a Loyds Tercentenary Foundation fellowship and by the Leverhulme Trust. H.E.H.'s research was supported by a Royal Society Wolfson merit award. We thank the CO<sub>2</sub>ReMoVe project who provided data and permitted publication. CO<sub>2</sub>ReMoVe is supported by the European Commission 6th Framework Program and by an industrial consortium (BP, Statoil, Wintershall, TOTAL, Schlumberger, DNV, ExxonMobil, ConocoPhillips, Vattenfall, and Vector). H. Mottram contributed to the pushdown analysis. Computational support and advice was provided by I. Frame, D. Lyness, C. Richardson, G. Roberts and J. Winterbourne. R. Arts, D. Lawton, and an anonymous referee wrote very helpful reviews. R.A.C. publishes with permission of the Executive Director of the British Geological Survey. Department of Earth Sciences contribution number ESC.2183.

## References

Alnes, H., O. Eiken, S. Nooner, G. Sasagawa, T. Stenvold, and M. Zumberge (2011), Results from Sleipner gravity monitoring: Updated density and temperature distribution of the CO<sub>2</sub> plume, *Energy Procedia*, *4*, 5504–5511.

Arts, R., O. Eiken, A. Chadwick, P. Zweigel, L. van der Meer, and B. Zinsaner (2004), Monitoring of CO<sub>2</sub> injected at Sleipner using time-lapse seismic data, *Energy*, *29*, 1383–1392.

Arts, R., O. Eiken, A. Chadwick, S. Thibeau, and S. Nooner (2008), Ten years' experience of monitoring CO<sub>2</sub> injection in the Utsira Sand at Sleipner, offshore Norway, *First Break*, *26*, 65–72.

Baklid, A., R. Korbøl, and G. Owren (1996), Sleipner Vest CO<sub>2</sub> disposal, CO<sub>2</sub> injection into a shallow underground aquifer, paper presented at SPE Annual Technical Conference and Exhibition, Soc. of Pet. Eng., Denver.

Bickle, M., A. Chadwick, H. Huppert, M. Hallworth, and S. Lyle (2007), Modelling carbon dioxide accumulation at Sleipner: Implications for underground carbon storage, *Earth Planet. Sci. Lett.*, *255*, 164–176.

Boait, F., N. White, R. Chadwick, D. Noy, and M. Bickle (2011), Layer spreading and dimming within the CO<sub>2</sub> plume at the Sleipner Field in the North Sea, *Energy Procedia*, *4*, 3254–3261.

Carcione, J., S. Picotti, D. Gei, and G. Rossi (2006), Physics and seismic modeling for monitoring CO<sub>2</sub> storage, *Pure Appl. Geophys.*, *163*, 175–207.

Chadwick, R. A., and D. J. Noy (2010), History: Matching flow simulations and time-lapse seismic data from the Sleipner CO<sub>2</sub> plume, in *From Mature Basins to New Frontiers: Proceedings of the 7th Petroleum Geology Conference Held at the Queen Elizabeth II Conference Centre, London 30 March-2 April 2009*, edited by B. A. Vining and S. C. Pickering, pp. 1171–1182, Geol. Soc., London.

Chadwick, R. A., P. Zweigel, U. Gregerson, G. Kirby, S. Holloway, and P. Johannessen (2004), Geological reservoir characterization of a CO<sub>2</sub> storage site: The Utsira Sand, Sleipner, northern North Sea, *Energy*, *29*, 1371–1381.

Chadwick, A., R. Arts, and O. Eiken (2005), 4D seismic quantification of a growing CO<sub>2</sub> plume at Sleipner, North Sea, in *Petroleum Geology: North-West Europe and Global Perspectives: Proceedings of the 6th Petroleum Geology Conference Held at the Queen Elizabeth II Conference Centre, London 6–9 October 2003*, edited by A. G. Dore and B. A. Vining, pp. 1385–1399, Geol. Soc., London.

Chadwick, R. A., D. J. Noy, R. Arts, and O. Eiken (2009a), Latest time-lapse seismic data from Sleipner yield new insights into CO<sub>2</sub> plume development, *Energy Procedia*, *1*, 2103–2110.

Chadwick, R. A., D. J. Noy, and S. Holloway (2009b), Flow processes and pressure evolution in aquifers during the injection of supercritical CO<sub>2</sub> as a greenhouse gas mitigation measure, *Pet. Geosci.*, *15*, 59–73.

Chadwick, R. A., et al. (2010), Quantitative analysis of time-lapse seismic monitoring data at the Sleipner CO<sub>2</sub> storage operation, *Leading Edge*, *29*, 170–177.

Galloway, W. E. (2002), Paleogeographic setting and depositional architecture of a sand-dominated shelf depositional system, Miocene Utsira formation North Sea basin, *J. Sediment. Res.*, *72*, 476–490.

Gassmann, F. (1951), Über die Elastizität poröser Medien, *Vierteljahresschr. der Naturf. Ges. in Zürich*, *96*, 1–23.

Golding, M. J., and H. Huppert (2010), The effect of confining impermeable boundaries on gravity currents in a porous medium, *J. Fluid Mech.*, *649*, 1–17.

Golding, M., J. Neufeld, M. Hesse, and H. Huppert (2011), Two-phase gravity currents in porous media, *J. Fluid Mech.*, *678*, 248–270.

Gregerson, U., (1998), Upper Cenozoic channels and fans on 3D seismic data in the northern Norwegian North Sea, *Pet. Geosci.*, *4*, 67–80.

Gregerson, U., O. Michelsen, and J. A. Sørensen (1997), Stratigraphy and facies distribution of the Utsira Formation and the Pliocene sequences in the northern North Sea, *Mar. Pet. Geol.*, *14*, 893–914.

Han, D., M. Sun, and M. Batzle (2010), CO<sub>2</sub> velocity measurement and models for temperatures up to 200°C and pressures up to 100 MPa, *Geophysics*, *75*, 123–129.

Head, M., J. Riding, and R. Chadwick (2004), Palynological and foraminiferal biostratigraphy of (Upper Pliocene) Nordland Group mudstones at Sleipner, northern North Sea, *Mar. Pet. Geol.*, *21*, 277–297.

Isaksen, D., and K. Tonstad (1989), A revised Cretaceous and Tertiary lithostratigraphic nomenclature for the Norwegian North Sea, *Bull. 5, Norw. Pet. Dir., Stavanger, Norway*.

Korbøl, R., and A. Kaddour (1996), Sleipner-Vest CO<sub>2</sub> disposal-injection of removed CO<sub>2</sub> into the Utsira Formation, *Energy Conv. Manage.*, *36*, 509–512.

Lindeberg, E., J. Vuillaume, and A. Ghaderi (2009), Determination of the CO<sub>2</sub> storage capacity of the Utsira formation, *Energy Procedia*, *1*, 2777–2784.

Lyle, S., H. Huppert, M. Hallworth, M. Bickle, and A. Chadwick (2005), Axisymmetric gravity currents in a porous medium, *J. Fluid Mech.*, *543*, 293–302.

Mavko, M., and T. Mukerji (1998), Bounds on low-frequency seismic velocities in partially saturated rocks, *Geophysics*, *63*, 918–924.

Neufeld, J., and H. Huppert (2009), Modelling carbon dioxide sequestration in layered strata, *J. Fluid Mech.*, *625*, 353–370.

- Neufeld, J., M. Hesse, A. Riaz, M. Hallworth, H. Tchelepi, and H. Huppert (2011a), Convective dissolution of carbon dioxide in saline aquifers, *Geophys. Res. Lett.*, *37*, L22404, doi:10.1029/2010GL044728.
- Neufeld, J., D. Vella, H. Huppert, and J. Lister (2011b), Leakage from gravity currents in a porous medium. Part 1. A localized sink, *J. Fluid Mech.*, *666*, 391–413.
- Nooner, S. K., O. Eiken, C. Hermanrud, G. S. Sasagawa, T. Stenvold, and M. A. Zumberge (2007), Constraints on the in situ density of CO<sub>2</sub> within the Utsira formation from time-lapse seafloor gravity measurements, *Int. J. Greenhouse Gas Control*, *1*, 198–214.
- Pritchard, D., A. Woods, and A. Hogg (2001), On the slow draining of a gravity current moving through a layered permeable medium, *J. Fluid Mech.*, *444*, 23–47.
- Singh, V., A. Cavanagh, H. Hansen, B. Nazarian, M. Iding, and P. Ringrose (2010), Reservoir modeling of CO<sub>2</sub> plume behavior calibrated against monitoring data from Sleipner, Norway, paper presented at SPE Annual Technical Conference and Exhibition, Soc. of Pet. Eng., Florence, Italy.
- Vella, D., and H. Huppert (2006), Gravity currents in a porous medium at an inclined plane, *J. Fluid Mech.*, *555*, 353–362.
- Zweigel, P., A. Lothe, R. Arts, and M. Hamburg (2000), Reservoir geology of the storage units in the Sleipner CO<sub>2</sub>-injection case: A contribution to the saline aquifer CO<sub>2</sub> storage project (SACS), *Rep. 23.4285.00/02/00*, Stiftelsen for Indust. og Tek. Forsk., Trondheim, Norway.
- Zweigel, P., et al. (2001), Results and experiences from the first Industrial-scale underground CO<sub>2</sub> sequestration case (Sleipner Field, North Sea), paper presented at AAPG Annual Meeting, Am. Assoc. of Pet. Geol., Denver.
- Zweigel, P., R. Arts, A. Lothe, and E. Lindeberg (2004), Reservoir geology of the Utsira Formation at the first industrial scale underground CO<sub>2</sub> storage site (Sleipner area, North Sea), *Geol. Soc. Spec. Publ.*, *233*, 165–180.
- 
- M. J. Bickle, F. C. Boait, and N. J. White, Bullard Laboratories, Madingley Rise, Madingley Road, Cambridge CB3 0EZ, UK. (mb72@cam.ac.uk; fcb27@cam.ac.uk; njw10@cam.ac.uk)
- R. A. Chadwick, British Geological Survey, Keyworth, Nottingham NG12 5GG, UK. (rach@bgs.ac.uk)
- H. E. Huppert and J. Neufeld, Institute of Theoretical Geophysics, Department of Applied Mathematics and Theoretical Physics, University of Cambridge, Centre for Mathematical Sciences, Wilberforce Road, Cambridge CB3 0WA, UK. (heh1@esc.cam.ac.uk; jn271@cam.ac.uk)